INTERNATIONAL TABLES FOR CRYSTALLOGRAPHY

Volume H

POWDER DIFFRACTION

Edited by

C. J. GILMORE, J. A. KADUK AND H. SCHENK

First Edition

Published for

THE INTERNATIONAL UNION OF CRYSTALLOGRAPHY

by

WILEY

2019

Contributing authors

A. J. ALLEN: National Institute of Standards and Technology (NIST), 100 Bureau Drive, Gaithersburg, MD 20899, USA. [5.8]

A. ALTOMARE: Institute of Crystallography – CNR, Via Amendola 122/o, Bari, I-70126, Italy. [3.4, 4.2]

G. ÁLVAREZ-PINAZO: Departamento de Química Inorgánica, Cristalografía y Mineralogía, Universidad de Málaga, 29071 Málaga, Spain, and X-Ray Data Services S.L., Edificio de institutos universitarios, c/ Severo Ochoa 4, Parque technológico de Andalucía, 29590 Málaga, Spain. [3.10]

M. A. G. ARANDA: ALBA Synchrotron, Carrer de la Llum 2–26, Cerdanyola, 08290 Barcelona, Spain, and Departamento de Química Inorgánica, Cristalografía y Mineralogía, Universidad de Málaga, 29071 Málaga, Spain. [3.10, 7.12]

R. ARLETTI: Dipartimento di Scienze della Terra, Università degli Studi di Torino, Via Valperga Caluso 35, I-10125 Torino, Italy. [7.14]

G. ARTIOLI: Dip. Geoscienze, Università di Padova, Via Gradenigo 6, I-35131 Padova, Italy. [7.4]

CH. BAERLOCHER: Laboratory of Crystallography, ETH Zurich, HCI, G 509, CH-8093 Zurich, Switzerland. [4.6]

G. BARR: Department of Chemistry, University of Glasgow, University Avenue, Glasgow G12 8QQ, UK. [3.8]

S. BATES: Triclinic Labs, 1201 Cumberland Ave., Suite S, West Lafayette, IN 47906, USA. [5.6]

W. VAN BEEK: Swiss–Norwegian Beamlines at ESRF, CS 40220, 38043 Grenoble Cedex 9, France. [2.9]

J. BERNSTEIN: Department of Chemistry, Ben-Gurion University of the Negev, PO Box 653, Beer Sheva, 84102, Israel. [7.5]

S. J. L. BILLINGE: Department of Applied Physics and Applied Mathematics, Columbia University, 500 West 120th Street, Room 200 Mudd, MC 4701, New York, NY 10027, USA, and Condensed Matter Physics and Materials Science Department, Brookhaven National Laboratory, PO Box 5000, Upton, NY 11973-5000, USA. [1.1, 5.7]

M. BIRKHOLZ: IHP, Im Technologiepark 25, 15236 Frankfurt (Oder), Germany. [5.4]

D. L. BISH: Department of Earth and Atmospheric Sciences, Indiana University, Bloomington, IN 47405, USA. [7.7]

D. BLACK: National Institute of Standards and Technology, Gaithersburg, Maryland, USA. [3.1]

K. CENZUAL: University of Geneva, 24 quai Ernest-Ansermet, CH-1211 Geneva 4, Switzerland. [3.7.5]

R. ČERNÝ: Laboratory of Crystallography, DQMP, University of Geneva, 24 quai Ernest-Ansermet, CH-1211 Geneva 4, Switzerland. [4.5]

D. CHATEIGNER: CRISMAT–ENSICAEN, UMR CNRS No. 6508, 6 Boulevard M. Juin, F-14050 Caen, France, and Normandie Université, IUT Mesures-Physiques, Université de Caen Normandie, Caen, France. [5.3]

J. P. CLINE: National Institute of Standards and Technology, Gaithersburg, Maryland, USA. [3.1]

G. CRUCIANI: Department of Physics and Earth Sciences, University of Ferrara, Polo Scientifico-technologico – Bld B, Via G. Saragat 1, I-44122 Ferrara, Italy. [7.14]

A. CUESTA: ALBA Synchrotron, Carrer de la Llum 2–26, Cerdanyola, 08290 Barcelona, Spain. [3.10]

C. CUOCCI: Institute of Crystallography – CNR, Via Amendola 122/o, Bari, I-70126, Italy. [3.4, 4.2]

W. I. F. DAVID: ISIS Facility, Rutherford Appleton Laboratory, Chilton OX11 0QX, UK. [4.3]

A. G. DE LA TORRE: Departamento de Química Inorgánica, Cristalografía y Mineralogía, Universidad de Málaga, 29071 Málaga, Spain. [3.10, 7.12]

R. E. DINNEBIER: Max Planck Institute for Solid State Research, Heisenbergstrasse 1, D-70569 Stuttgart, Germany. [1.1, 4.8]

W. DONG: Department of Chemistry, University of Glasgow, University Avenue, Glasgow G12 8QQ, UK. [3.8]

H. EHRENBERG: Institut für Angewandte Materialien (IAM-ESS), Karlsruhe Institut für Technologie (KIT), Eggenstein-Leopoldshafen, Germany. [2.8]

V. FAVRE-NICOLIN: ESRF – The European Synchrotron, F-38043 Grenoble, France. [4.5]

F. R. FERET‡: Feret Analytical Consulting, 128, Des Fauvettes, Saint-Colomban, Québec, Canada J5K 0E2. [7.6]

G. FERRARIS: Dipartimento di Scienze della Terra, Università degli Studi di Torino, Via Valperga Caluso 35, I-10125 Torino, Italy. [7.14]

A. FITCH: ESRF, 71 Avenue des Martyrs, CS40220, 38043 Grenoble Cedex 9, France. [2.2]

A. J. FLORENCE: Strathclyde Institute of Pharmacy and Biomedical Sciences, University of Strathclyde, Glasgow, UK. [4.4]

H. FUESS: Technische Universität Darmstadt, Darmstadt, Germany. [2.8]

M. GARCÍA-MATÉ: Departamento de Química Inorgánica, Cristalografía y Mineralogía, Universidad de Málaga, 29071 Málaga, Spain, and X-Ray Data Services S.L., Edificio de institutos universitarios, c/ Severo Ochoa 4, Parque technológico de Andalucía, 29590 Málaga, Spain. [3.10]

C. J. GILMORE: Department of Chemistry, University of Glasgow, University Avenue, Glasgow G12 8QQ, UK. [3.8, 6.1]

T. E. GORELIK: University of Ulm, Central Facility for Electron Microscopy, Electron Microscopy Group of Materials Science (EMMS), Albert Einstein Allee 11, 89069 Ulm, Germany. [2.4]

S. GRAŽULIS: Institute of Biotechnology, Vilnius University, Sauletekio al. 7, 10257 Vilnius, Lithuania. [3.7.8]

B. B. HE: Bruker AXS Inc., 5465 E. Cheryl Parkway, Madison, WI 53711, USA. [2.5]

A. HENINS: National Institute of Standards and Technology, Gaithersburg, Maryland, USA. [3.1]

M. HINTERSTEIN: Institut für Angewandte Materialien (IAM-ESS), Karlsruhe Institut für Technologie (KIT), Eggenstein-Leopoldshafen, Germany. [2.8]

C. J. HOWARD: School of Engineering, University of Newcastle, Callaghan, NSW 2308, Australia. [2.3]

QINGZHEN HUANG: NIST Center for Neutron Research, National Institute of Standards and Technology, Gaithersburg, Maryland 20899, USA. [7.13]

A. HUQ: Chemical and Engineering Materials Division, Spallation Neutron Source, PO Box 2008, MS 6475, Oak Ridge, TN 37831, USA. [2.10]

J. A. KADUK: Department of Chemistry, Illinois Institute of Technology, 3101 South Dearborn Street, Chicago, IL 60616, USA, Department of Physics, North Central College, 131 South Loomis Street, Naperville, IL 60540, USA, and Poly Crystallography Inc., 423 East Chicago Avenue, Naperville, IL 60540, USA. [2.10, 3.7, 4.9, 6.1, 7.11]

‡ Emeritus, Senior Consultant with Arvida R&D Centre of Rio Tinto Alcan in Jonquiere, Quebec, Canada.

A. Katrusiak: Faculty of Chemistry, Adam Mickiewicz University, Poznań, Poland. [2.7]

A. Kern: Bruker AXS, Östliche Rheinbrückenstrasse 49, Karlsruhe 76187, Germany. [2.1]

E. H. Kisi: School of Engineering, University of Newcastle, Callaghan, NSW 2308, Australia. [2.3]

R. Kleeberg: TU Bergakademie Freiberg, Institut für Mineralogie, Brennhausgasse 14, Freiberg, D-09596, Germany. [3.9]

K. Knorr: Bruker AXS GmbH, Oestliche Rheinbrückenstr. 49, 76187 Karlsruhe, Germany. [3.9]

U. Kolb: Institut für Physikalische Chemie, Johannes Gutenberg-Universität Mainz, Welderweg 11, 55099 Mainz, Germany. [2.4]

J. L. Lábár: Institute of Technical Physics and Materials Science, Centre for Energy Research, Hungarian Academy of Sciences, Konkoly Thege M. u. 29–33, H-1121 Budapest, Hungary. [2.4]

A. Le Bail: Université du Maine, Institut des Molécules et Matériaux du Mans, UMR CNRS 6283, Avenue Olivier Messiaen, 72085 Le Mans Cedex 9, France. [3.5]

L. León-Reina: Servicios Centrales de Apoyo a la Investigación, Universidad de Málaga, 29071 Málaga, Spain. [3.10, 7.12]

M. Leoni: Department of Civil, Environmental and Mechanical Engineering, University of Trento, via Mesiano 77, 38123 Trento, Italy. [3.6, 5.1]

L. Lutterotti: Dipartimento di Ingegneria Industriale, Università di Trento, via Sommarive, 9, 38123 Trento, Italy. [5.3]

L. B. McCusker: Laboratory of Crystallography, ETH Zurich, HCI, G 509, CH-8093 Zurich, Switzerland. [4.6]

I. C. Madsen: CSIRO Mineral Resources, Private Bag 10, Clayton South 3169, Victoria, Australia. [3.9]

O. V. Magdysyuk: Max Planck Institute for Solid State Research, Heisenbergstrasse 1, D-70569 Stuttgart, Germany. [4.8]

I. Margiolaki: Department of Biology, Section of Genetics, Cell Biology and Development, University of Patras, GR-26500, Patras, Greece. [7.1]

M. H. Mendenhall: National Institute of Standards and Technology, Gaithersburg, Maryland, USA. [3.1]

S. T. Misture: Inamori School of Engineering, Alfred University, Alfred, NY 14802, USA. [7.9]

A. Moliterni: Institute of Crystallography – CNR, Via Amendola 122/o, Bari, I-70126, Italy. [3.4, 4.2]

M. Morales: CIMAP ENSICAEN, UMR CNRS No. 6252, 6 Boulevard M. Juin, F-14050 Caen, France, and Normandie Université, ESPE Caen, Université de Caen Normandie, Caen, France. [5.3]

P. Pattison: Laboratory for Quantum Magnetism, Institute of Physics, Ecole Polytechnique Federale de Lausanne, CH-1015 Lausanne, Switzerland. [2.9]

N. C. Popa: National Institute of Materials Physics, Atomistilor Str. No. 405A, PO Box MG7, 077125 Magurele, Romania. [5.2]

H. F. Poulsen: Institut for Fysik, Danmarks Tekniske Universitet, Kgs. Lyngby, Denmark. [5.5]

C. A. Reiss: Noordikslaan 51, 7602 CC Almelo, The Netherlands. [2.6]

D. F. Rendle‡: Cranfield Forensic Institute, Department of Engineering & Applied Science, Cranfield University, Shrivenham, Swindon SN6 8LA, Wiltshire, UK. [7.2]

S. M. Reutzel-Edens: Lilly Research Laboratories, Eli Lilly & Company, Indianapolis, IN 46285, USA. [7.5]

R. Rizzi: Institute of Crystallography – CNR, Via Amendola 122/o, Bari, I-70126, Italy. [3.4, 4.2]

M. A. Rodriguez: Materials Characterization and Performance Department, Sandia National Laboratories, Albuquerque, NM 87185–1411, USA. [7.3]

I. Santacruz: Departamento de Química Inorgánica, Cristalografía y Mineralogía, Universidad de Málaga, 29071 Málaga, Spain. [3.10]

N. V. Y. Scarlett: CSIRO Mineral Resources, Private Bag 10, Clayton South 3169, Victoria, Australia. [3.9, 7.7]

H. Schenk: HIMS, FWNI, University of Amsterdam, Postbus 94157, 1090 GD Amsterdam, The Netherlands. [6.1]

M. U. Schmidt: Institut für Anorganische und Analytische Chemie, Johann Wolfgang Goethe-Universität, Max-von-Laue-Strasse, D-60438 Frankfurt am Main, Germany. [7.10]

A. Senyshyn: Technische Universität München, Garching b. München, Germany. [2.8]

K. Shankland: School of Pharmacy, The University of Reading, Whiteknights, PO Box 224, Reading RG6 6AD, UK. [4.1]

S. van Smaalen: Laboratory of Crystallography, University of Bayreuth, Universitätsstrasse 30, D-95447 Bayreuth, Germany. [4.8]

K. Ståhl: Department of Chemistry, Technical University of Denmark, Kemitorvet, Building 207, DK-2800 Kgs. Lyngby, Denmark. [3.7.7.2]

J. K. Stalick: NIST Center for Neutron Research, National Institute of Standards and Technology, 100 Bureau Drive, Gaithersburg, MD 20899, USA. [4.9.3]

P. W. Stephens: Department of Physics and Astronomy, Stony Brook University, Stony Brook, NY 11794–3800, USA. [3.2]

B. H. Toby: Advanced Photon Source, Argonne National Laboratory, Argonne, IL 60439-4856, USA. [4.7, 4.9.2, 4.9.3, 4.10]

O. Vallcorba: ALBA Synchrotron, Carrer de la Llum 2–26, Cerdanyola, 08290 Barcelona, Spain. [3.10]

G. B. M. Vaughan: European Synchrotron Radiation Facility, Grenoble, France. [5.5]

P. Villars: 400 Schwanden, Vitznau, CH-6354 Switzerland. [3.7.5]

R. B. Von Dreele: Advanced Photon Source, Argonne National Laboratory, 9700 S. Cass Avenue, Argonne, IL 60439–4814, USA. [3.3]

P. S. Whitfield: Energy, Mining and Environment Portfolio, National Research Council Canada, 1200 Montreal Road, Ottawa ON K1A 0R6, Canada. [2.10]

D. Windover: National Institute of Standards and Technology, Gaithersburg, Maryland, USA. [3.1]

W. Wong-Ng: Materials Science Measurement Division, National Institute of Standards and Technology, Gaithersburg, MD 20899, USA. [7.8]

J. Zhang: Intel Corporation, Technology Manufacturing Group, 2501 NE Century Boulevard, Hillsboro, OR 97124, USA. [2.4]

J.-M. Zuo: Department of Materials Science and Engineering, University of Illinois, 1304 W. Green Street, Urbana, IL 61801, USA. [2.4]

‡ Visiting Fellow.

Contents

PAGE

Preface

International Tables for Crystallography started life in in 1935 as a two-volume set entitled *Internationale Tabellen zur Bestimmung von Kristallstrukturen*, with C. Hermann as editor. We are now in the third series, with eight volumes covering all aspects of crystallography from symmetry to macromolecular crystallography. However, there has always been one glaring omission and one that has become increasingly serious: powder diffraction. This is odd: powder crystallography started as early as 1916 with the seminal work of Debye and Scherrer, and has grown to include quantitative and semi-quantitative analysis, structure solution and refinement, two-dimensional data, comprehensive databases, clustering, and microstructural properties, and is applied to a wide range of problems of both academic and industrial interest. Articles in the International Union of Crystallography's monthly *Journal of Applied Crystallography* are dominated by powder-diffraction papers. In terms of instrumentation, there are more powder diffractometers (~10 000) in use worldwide than any other comparable diffraction instrument. There have also been rapid advances in radiation sources and detectors, and major developments in software, computing power and visualization tools, all of which have made what was once cutting-edge science commonplace.

The methodology that has done more than anything to transform the field treats the measured powder-diffraction data in a comparable way to single-crystal data (albeit with more restrictive conditions) and is generally known as Rietveld refinement. This method will be found everywhere in this volume and was developed in the 1960s by Bert Loopstra (who came up with the concept), Bob van Laar (who worked out the mathematics) and Hugo Rietveld (who wrote the first computer program for it), as discussed in a recent article by van Laar & Schenk [*Acta Cryst.* (2018), A**74**, 88–92].

The field has not been devoid of books: there are excellent books edited by Dinnebier and Billinge [*Powder Diffraction Theory and Practice* (2008), Cambridge: Royal Society of Chemistry], Clearfield, Reibenspies and Bhuvanesh [*Principles and Applications of Powder Diffraction* (2008), Oxford: Wiley] and Mittemeijer and Welzel [*Modern Diffraction Methods* (2013), Weinheim: Wiley-VCH]. These, however, are not completely comprehensive and the need for a volume of *International Tables* dedicated to powder diffraction has become increasingly urgent.

So here it is. As if to emphasize the scale and diversity of the topic, it is one of the larger volumes of *International Tables* with over 900 pages and 54 chapters. The first part is devoted to basic diffraction theory as applied to powder samples, followed by parts on instrumentation and sample preparation, methodology, structure determination, defects, texture and microstructure, and software, and concluding with descriptions of applications over a wide variety of disciplines ranging from ceramics to pharmaceuticals. Even a volume of this size cannot be wholly comprehensive, but the editors hope that it covers a wide range of topics that will be relevant and of interest to most powder diffractionists. We plan to include yet more topics in a second edition.

The volume is intended primarily to be a practical one – when you have a problem in powder analysis this should be the first book you reach for. To this end, the data for many of the examples discussed in the text can be downloaded from https://it.iucr.org, so that readers can try the examples for themselves. We have not (yet) included step-by-step instructions on how to process the data; perhaps that will come in the future. The chapter on software gives information on how to obtain the necessary programs.

A word is needed about notation. A field as diverse as powder diffraction does not have a uniform notation. Texture and stress, for example, use a different nomenclature to structure solution. Our conclusion was that if we were to attempt to impose a uniform notation throughout the volume, it would have made it very difficult to link the chapters to the existing literature. We have to live with diversity.

An enterprise such as this has been a large undertaking, and we thank the authors for their patience. It is important to acknowledge the role of the staff at the IUCr offices in Chester, especially Nicola Ashcroft, Simon Glynn and Peter Strickland. We are very grateful for all their hard work.

Chris Gilmore, Jim Kaduk and Henk Schenk
Editors, *International Tables for Crystallography* Volume H

SAMPLE PAGES

(2006), Fewster (2003), Bowen & Tanner (1998), Jenkins & Snyder (1996), Klug & Alexander (1974), and Peiser *et al.* (1955). An extensive discussion of the principles of combining X-ray optics to optimally suit a wide range of different powder diffraction as well as thin-film applications has been given in the textbook by Fewster (2003).

2.1.6.3.1. *Absorptive X-ray optics*

2.1.6.3.1.1. Apertures

The simplest way of beam conditioning is to place apertures such as slits (line focus) or pinholes (point focus) into the incident and/or diffracted beam to control beam divergence and shape, and to reduce unwanted scattering from air or any beam-path components. Apertures are 'shadow-casting' optics and thus cannot increase flux density. Reducing beam divergence and beam dimensions by means of apertures invariably results in a loss of intensity that is inversely proportional to the slit aperture.

The principles are shown in Fig. 2.1.14. The divergence of a beam is established by the dimensions of the focal spot as well as the aperture and the distance of the aperture from the source (Fig. 2.1.14*a*). The divergence in the diffraction plane is usually called 'equatorial divergence' and the divergence in the axial direction 'axial divergence'. Apertures can be of the plug-in type requiring manual changes of the aperture to obtain different divergence angles, or – usually only for equatorial divergence slits – motorized. Motorized slits are mostly used in the Bragg–Brentano geometry to limit equatorial divergence, which can be arbitrarily chosen and either be kept constant to keep the diffracting specimen volume constant (as is invariably the case with plug-in slits), or varied as a function of 2θ to keep the illuminated specimen length constant. Typical aperture angles range from 0.1–1°.

To provide additional collimation, a second aperture may be placed at some distance away from the first (Fig. 2.1.14*b*). When using the same aperture, an almost-parallel beam may be obtained from a divergent beam at the cost of high intensity losses. A third aperture is often used to reduce scattering by the second slit. In laboratory X-ray diffractometers dedicated for SAXS analysis such collimation systems may reach lengths of more than 1 m.

Another way to parallelize radiation is to use a parallel-plate collimator (PPC), which is manufactured from sets of parallel, equally spaced thin metal plates, as shown in Fig. 2.1.14(*c*). Each pair of neighbouring plates works like a double-aperture arrangement as shown in Fig. 2.1.14(*b*). In contrast to simple slits and pinholes, PPCs do not change the shape of the beam. PPCs arranged parallel to the diffraction plane are usually called 'Soller slits' and are used to control axial divergence. Such devices can be used for focusing as well as parallel-beam geometries with typical aperture angles ranging from 1–5°. Soller slits are usually mounted on both the incident- and diffracted-beam sides of the specimen. PPCs arranged parallel to the diffraction plane are specifically used in parallel-beam geometries to minimize equatorial beam divergence, with typical aperture angles ranging from 0.1–0.5°.

The ways in which the diffracted beam can be conditioned are limited when employing one- or two-dimensional detectors. A particular issue related to these types of detectors is unwanted scattering from air or any beam-path components. Ideally, a closed, evacuated or He-flushed beam path will be used, but this is often not feasible owing to collision issues. For smaller detectors it is possible to place the anti-scatter aperture closer to the specimen surface. Alternatively, a knife edge may be placed on top of the specimen. As knife edges may interfere with divergent beams at higher 2θ angles, it is necessary to move them away from the specimen at higher 2θ angles. Another possibility, limited to one-dimensional detectors, is to use radial Soller slits as shown in Fig. 2.1.14(*d*).

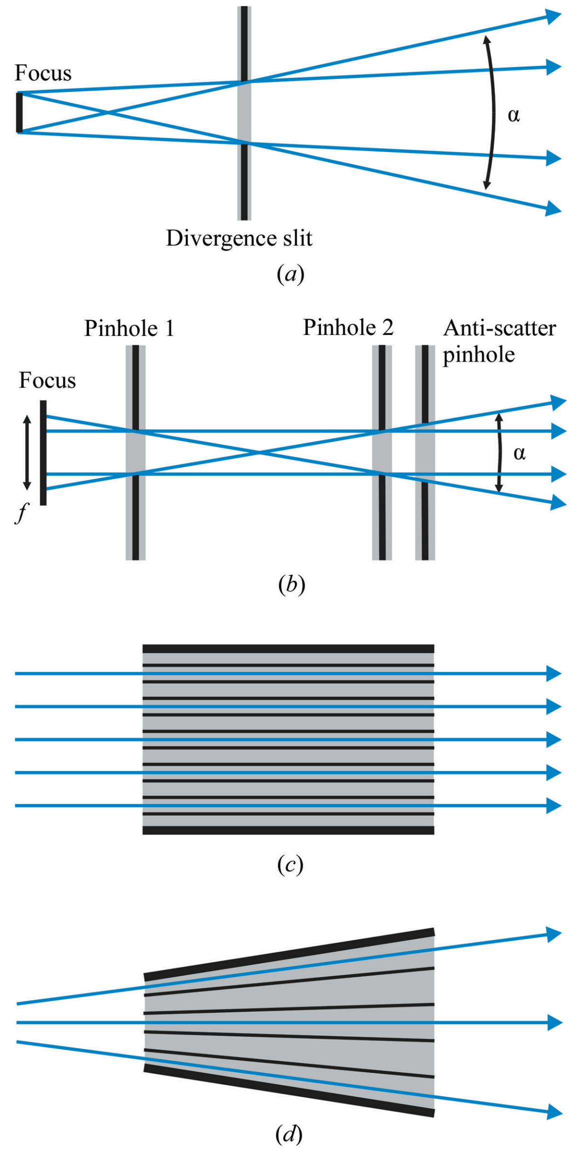

Figure 2.1.14
Apertures used for beam collimation. α: divergence angle, *f*: virtual focus. (*a*) Single slit or pinhole, (*b*) parallelization through double slits or pinholes, (*c*) parallelization through a parallel-plate collimator, (*d*) a radial plate collimator.

2.1.6.3.1.2. Metal filters

Metal filters are the most frequently used devices for monochromatization of X-rays in laboratory diffractometers. Metal filters represent single-band bandpass devices where monochromatization is based on the *K* absorption edge of the filter material to selectively allow transmission of the $K\alpha$ characteristic lines while filtering white radiation, $K\beta$ radiation (hence they are frequently known as '$K\beta$ filters'), and other characteristic lines.

A properly selected metal filter has its *K* absorption edge right between the energies of the $K\alpha$ and $K\beta$ characteristic lines of the source. As a rule of thumb, this is achieved by choosing an element just one atomic number less than the X-ray source target material in the periodic table. For heavy target materials such as

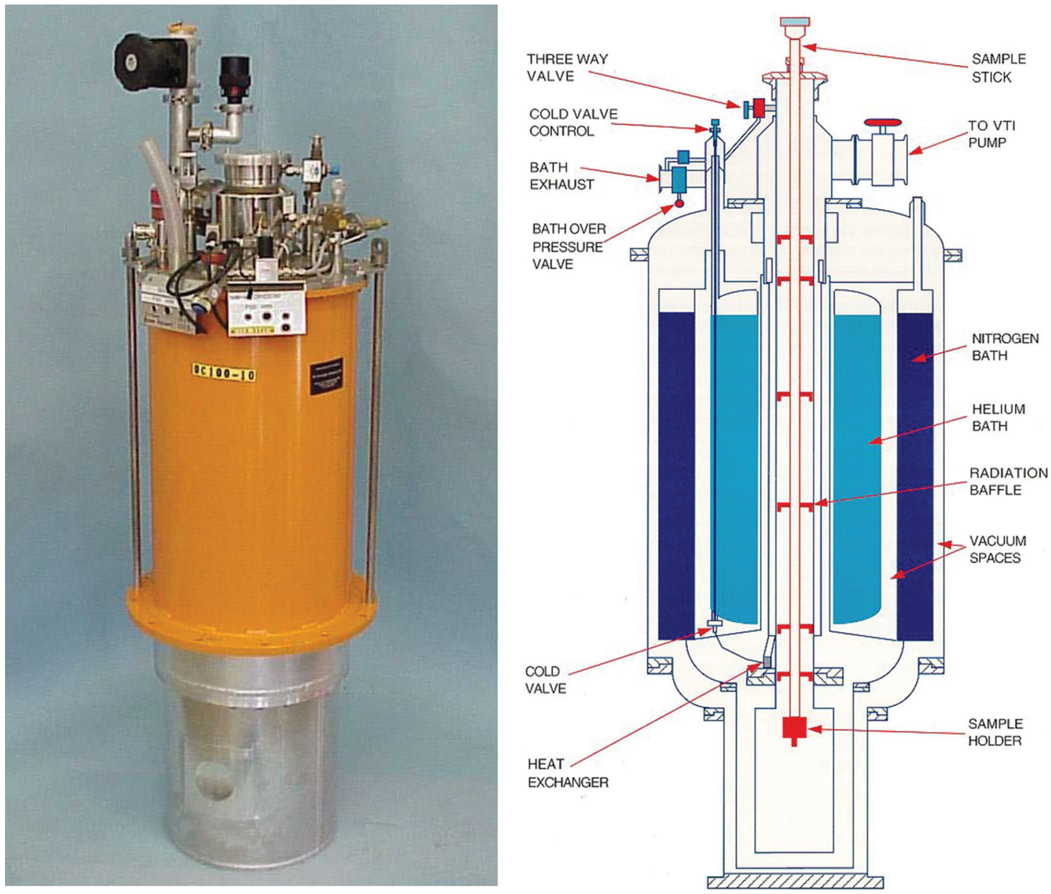

(a) (b)

Figure 2.3.26
(a) Exterior and (b) interior of the standard ILL liquid-helium cryostat for cooling samples in the range 1.8–295 K. An internal heater allows samples to be studied without interruption from 1.8–430 K. Reproduced with permission from the ILL.

cylindrical sections that allow ready transmission of neutrons but preserve the vacuum and exclude radiant heat from the outside world. Liquid-helium cryostats can generally attain base temperatures of 4.2 K (He alone) or 1.9 K if pumped. Liquid-nitrogen cryostats are limited to 77 K. A second type of low-temperature device is the closed-cycle He refrigerator, commonly referred to by the trade name Displex. These are more compact than a liquid-helium cryostat and do not require refilling. Depending on the number of stages and internal design, refrigerators with base temperatures as low as 4 K are available.

Samples are typically first cooled to base temperature and then studied at the chosen sequence of increasing temperatures. This is achieved through a small electric resistance heater and control system. As heat transfer to and from the sample is deliberately poor in these devices, sufficient time should be allowed for the (often large) sample to reach thermal equilibrium before recording its neutron-diffraction pattern. It is worth noting that the attainment of thermal equilibrium does not guarantee that the sample has attained thermodynamic equilibrium. Some phase transitions are notoriously slow, for example the ordering of hydrogen (or deuterium) in Pd metal at 55 K and 75 K, which can take up to a month (Kennedy *et al.*, 1995; Wu *et al.*, 1996), or the ordering of C in TiC_x ($0.6 < x < 0.9$) around 973 K, which can take a week to complete (Moisy-Maurice *et al.*, 1982; Tashmetov *et al.*, 2002).

Raising samples to above ambient temperature is, for X-ray diffraction, the subject of a separate chapter (Chapter 2.6); however, neutron-diffraction high-temperature devices are somewhat different. Most commonly used and most versatile is the foil element resistance furnace, in which Cu bus bars transfer electric current to a cylindrical metal foil which heats up as a result of its electrical resistance. Foil elements are typically 30–60 mm in diameter and up to 200 or 250 mm long so as to provide a long hot zone of uniform temperature within the furnace. The sample is located, *via* a sample stick from above or occasionally *via* a pedestal support from below, in the centre of the foil heating element, ensuring that it is uniformly bathed in radiant heat. Concentric metal-foil heat shields greatly reduce heat loss to the exterior by radiation, while convective losses are avoided by evacuating the interior of the furnace to $\sim 10^{-5}$ mbar. Metals for manufacture of the foil elements include V, which has almost no coherent diffraction pattern and can operate continuously up to 1173 K or intermittently to 1273 K. For temperatures above this, progressively more refractory metals are chosen such as Nb (<1773 K), Ta (<2473 K) or W (2773 K). These materials will contribute some small diffraction peaks to the observed patterns, which requires the recording of reference patterns from the empty furnace before commencing. Owing to the internal vacuum, some types of sample are at risk of subliming, decomposing or disproportioning during the experiment. In such cases, sample cans that extend outside the hot zone, where they can be coupled to a gas-handling system and filled with an internal atmosphere of air, an inert gas or a reactive gas of interest as required, are used.

Alternatives to foil furnaces include variations of the wire-wound laboratory furnace with a split winding and reduced insulating material in the neutron beam path, Peltier devices, hot-air blowers and induction heaters. The first three of these are discussed by Kisi & Howard (2008).

where $F(x, y)$ is the flux (in photons s^{-1}) intercepted by the pixel and B is the brightness of the source (in photons s^{-1} $mrad^{-2}$) or scattering from the sample. The ratio of the flux in pixel $P(x, y)$ to that in the centre pixel $P(0, 0)$ is then given as

$$\frac{F(x,y)}{F(0,0)} = \frac{D^3}{R^3} = \frac{D^3}{(D^2+x^2+y^2)^{3/2}} = \cos^3\phi, \qquad (2.5.20)$$

where ϕ is the angle between the X-rays to the pixel $P(x, y)$ and the line from S to the detector in perpendicular direction. It can be seen that the greater the sample-to-detector distance, the smaller the difference between the centre pixel and the edge pixel in terms of the flux from the homogeneous source. This is the main reason why a data frame collected at a short sample-to-detector distance has a higher contrast between the edge and centre than one collected at a long sample-to-detector distance.

2.5.3.2.2. *Spatial resolution of area detectors*

In a 2D diffraction frame, each pixel contains the X-ray intensity collected by the detector corresponding to the pixel element. The pixel size of a 2D detector can be determined by or related to the actual feature sizes of the detector structure, or artificially determined by the readout electronics or data-acquisition software. Many detector techniques allow multiple settings for variable pixel size, for instance a frame of 2048 $\times$ 2048 pixels or 512 $\times$ 512 pixels. Then the pixel size in 512 mode is 16 (4 $\times$ 4) times that of a pixel in 2048 mode. The pixel size of a 2D detector determines the space between two adjacent pixels and also the minimum angular steps in the diffraction data, therefore the pixel size is also referred to as pixel resolution.

The pixel size does not necessarily represent the true spatial resolution or the angular resolution of the detector. The resolving power of a 2D detector is also limited by its point-spread function (PSF) (Bourgeois *et al.*, 1994). The PSF is the two-dimensional response of a 2D detector to a parallel point beam smaller than one pixel. When the sharp parallel point beam strikes the detector, not only does the pixel directly hit by the beam record counts, but the surrounding pixels may also record some counts. The phenomenon is observed as if the point beam has spread over a certain region adjacent to the pixel. In other words, the PSF gives a mapping of the probability density that an X-ray photon is recorded by a pixel in the vicinity of the point where the X-ray beam hits the detector. Therefore, the PSF is also referred to as the spatial redistribution function. Fig. 2.5.12(*a*) shows the PSF produced from a parallel point beam. A plane at half the maximum intensity defines a cross-sectional region within the PSF. The FWHM can be measured at any direction crossing the centroid of the cross section. Generally, the PSF is isotropic, so the FWHMs measured in any direction should be the same.

Measuring the PSF directly by using a small parallel point beam is difficult because the small PSF spot covers a few pixels and it is hard to establish the distribution profile. Instead, the line-spread function (LSF) can be measured with a sharp line beam from a narrow slit (Ponchut, 2006). Fig. 2.5.12(*b*) is the intensity profile of the image from a sharp line beam. The LSF can be obtained by integrating the image from the line beam along the direction of the line. The FWHM of the integrated profile can be used to describe the LSF. Theoretically, LSF and PSF profiles are not equivalent, but in practice they are not distinguished and may be referenced by the detector specification interchangeably. For accurate LSF measurement, the line beam is intentionally positioned with a tilt angle from the orthogonal direction of the pixel array so that the LSF can have smaller steps in the integrated profile (Fujita *et al.*, 1992).

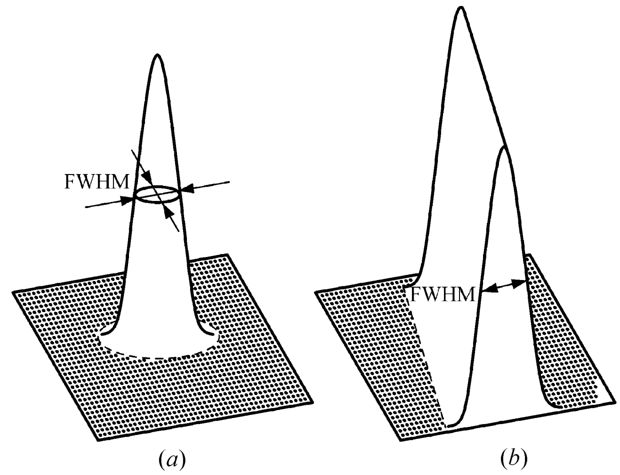

Figure 2.5.12
(*a*) Point-spread function (PSF) from a parallel point beam; (*b*) line-spread function (LSF) from a sharp line beam.

The RMS (root-mean-square) of the distribution of counts is another parameter often used to describe the PSF. The normal distribution, also called the Gaussian distribution, is the most common shape of a PSF. The RMS of a Gaussian distribution is its standard deviation, σ. Therefore, the FWHM and RMS have the following relation, assuming that the PSF has a Gaussian distribution:

$$\text{FWHM} = 2[-2\ln(1/2)]^{1/2}\text{RMS} = 2.3548 \times \text{RMS}. \qquad (2.5.21)$$

The values of the FWHM and RMS are significantly different, so it is important to be precise about which parameter is used when the value is given for a PSF.

For most area detectors, the pixel size is smaller than the FWHM of the PSF. The pixel size should be small enough that at least a 50% drop in counts from the centre of the PSF can be observed by the pixel adjacent to the centre pixel. In practice, an FWHM of 3 to 6 times the pixel size is a reasonable choice if use of a smaller pixel does not have other detrimental effects. A further reduction in pixel size does not necessarily improve the resolution. Some 2D detectors, such as pixel-array detectors, can achieve a single-pixel PSF. In this case, the spatial resolution is determined by the pixel size.

2.5.3.2.3. *Detective quantum efficiency and energy range*

The detective quantum efficiency (DQE), also referred to as the detector quantum efficiency or quantum counting efficiency, is measured by the percentage of incident photons that are converted by the detector into electrons that constitute a measurable signal. For an ideal detector, in which every X-ray photon is converted to a detectable signal without additional noise added, the DQE is 100%. The DQE of a real detector is less than 100% because not every incident X-ray photon is detected, and because there is always some detector noise. The DQE is a parameter defined as the square of the ratio of the output and input signal-to-noise ratios (SNRs) (Stanton *et al.*, 1992):

$$\text{DQE} = \left(\frac{(S/N)_{\text{out}}}{(S/N)_{\text{in}}}\right)^2. \qquad (2.5.22)$$

The DQE of a detector is affected by many variables, for example the X-ray photon energy and the counting rate. The dependence of the DQE on the X-ray photon energy defines the

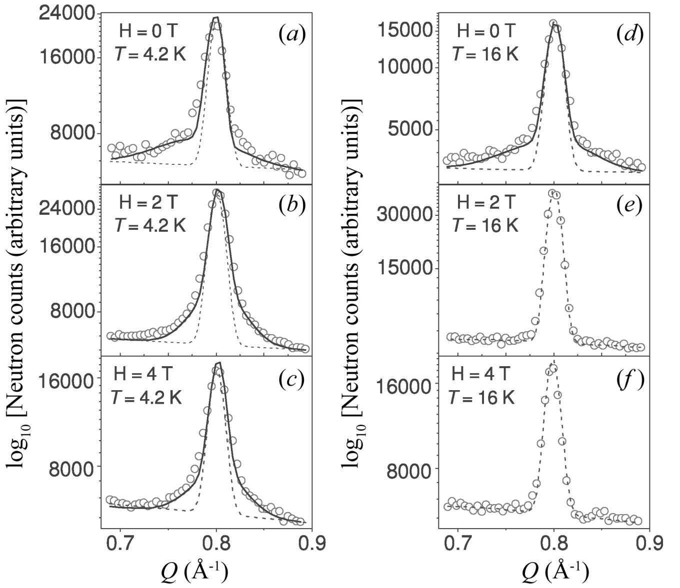

Figure 2.8.15
The observed Bragg reflection 100 (open circles) under an applied field of (*a*) 0 T, (*b*) 2 T and (*c*) 4 T at 4.2 K and (*d*) 0 T, (*e*) 2 T and (*f*) 4 T at 16 K (taken from Yusuf *et al.*, 2013). Copyright IOP Publishing. Reproduced with permission. All rights reserved.

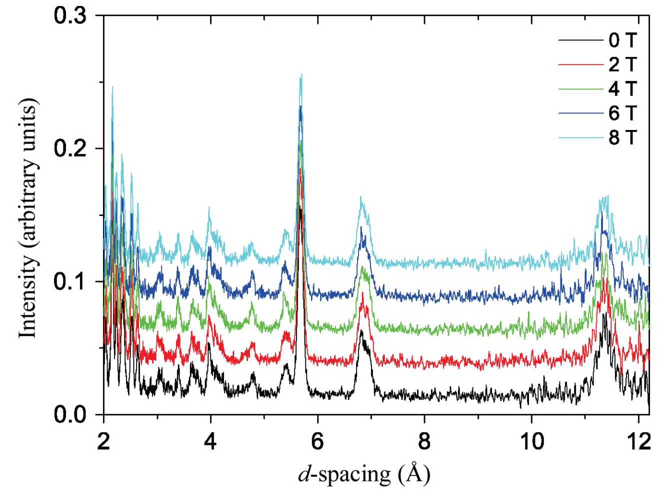

Figure 2.8.16
Time-of-flight diffraction patterns of YMn_2O_5 at 1.6 K under magnetic fields between 0 and 8 T (taken from Radaelli & Chapon, 2008). Copyright IOP Publishing. Reproduced with permission. All rights reserved.

narrow temperature range a macroscopic polar vector leads to a multiferroic behaviour. As this study was based on single-crystal neutron measurements, no further details are given here. Frustrated triangular-lattice Ising antiferromagnets have degenerate magnetic ground states, which give rise to very complex magnetic structures. As there are only small differences in the competing exchange interaction in such frustrated triangular-lattice compounds, a sequence of phase transitions is introduced by changes in temperature or magnetic field. The compound $Ca_3Co_2O_6$ is another example of a frustrated system. Field-dependent powder diffraction patterns were reported for the doped system $Ca_3Co_{1.8}Fe_{0.2}O_6$ by Yusuf *et al.* (2013). They distinguished the short-range magnetic order (SRO), reflected in the half-width of the Bragg reflections (Fig. 2.8.15), from the long-range order as given by the Bragg positions. They stated that even under magnetic fields up to 4 T the broadening of Bragg reflections indicates the persistence of SRO. In a field of 2 T, the observed change in the structure from incommensurate to commensurate indicates a reduction of spin frustration. In fields of 4 T, a ferrimagnetic system is introduced, followed by a ferromagnetic one above 5 T.

2.8.3.3.2.2. *Manganite systems*

Like the vanadates, in the class of rare-earth manganites of the type RMn_2O_5 successive magnetic phase transitions between commensurate (CO) and incommensurate phases (ICP) can occur. Intensive investigations have been undertaken to understand the relationship between their magnetic and dielectric properties. The spontaneous electric polarization is induced by a magnetic transition. Thus the primary order parameter is magnetic rather than structural. Among the rare-earth compounds, those containing Nd or an element lighter than Nd do not exhibit ferroelectricity. In all these materials a broken magnetic symmetry at lower temperatures leads to a polar symmetry group. In addition, a cycloidal component indicates a common underlying mechanism. The Mn^{3+} and Mn^{4+} ions are fully charge-ordered. Neutron diffraction studies of these phases have been performed by Radaelli & Chapon (2008), who also analysed the possible exchange pathways. In $TbMn_2O_5$ the *H*–*T* phase diagram of the commensurate–low-temperature–incommensurate (CO–LT–ICP) magnetic transitions shows an upward jump in the transition temperature from ~25 K at zero field to 27 K at 9 T. The low-temperature ICP phase is stabilized under an external field for $TbMn_2O_5$ and the dielectric constant is enhanced. It was concluded that Tb and Mn order independently, implying the absence of coupling terms between them. Strong support for this suggestion was provided by an in-field neutron study on the analogue YMn_2O_5. Neither the positions nor the intensities of the magnetic Bragg reflections were affected by the magnetic field (Fig. 2.8.16). The magnetic low-temperature ICP phase in the Tb compound was stabilized under a magnetic field. This is in contrast to observations on $HoMn_2O_5$ by Kimura *et al.* (2007), using single crystals. In both cases, however, the neutron data correlate directly with the results obtained by dielectric measurements under a magnetic field. The difference in the behaviours is thus confirmed. The two studies also reveal different magnetic order at low temperatures. The same magnetic sequence at low temperatures as for Tb was observed in YMn_2O_5, which does not contain a magnetic rare-earth element. Under fields up to 8 T the positions and the intensities of the magnetic Bragg reflections remained unchanged, showing that the antiferromagnetic structure of the manganese sublattice is extremely stable. As in the vanadates, the main reason for the sequence of magnetic structures is frustration of the manganese spins. Without going too deeply into the details of the different exchange pathways and orbital occupancies, one factor behind this behaviour is the Jahn–Teller effect of the Mn^{3+} ion, which is also relevant in the multiferroic $TbMnO_3$ as part of the $RMnO_3$ family (Kimura *et al.*, 2003). Another feature often found in multiferroic systems is the small ferromagnetic component caused by small spin canting due to Dzyaloshinskii–Moriya interactions. This property strongly influences the low-temperature magnetism in RMn_2O_5 (Kimura *et al.*, 2009).

2.8.3.3.3. *Additional systems and scattering techniques*

Information about the anisotropy of the local magnetic susceptibility at different magnetic sites has been extracted from diffraction patterns for a $Tb_2Sn_2O_7$ powder measured using polarized neutrons under magnetic fields of 1 and 5 T (Gukasov

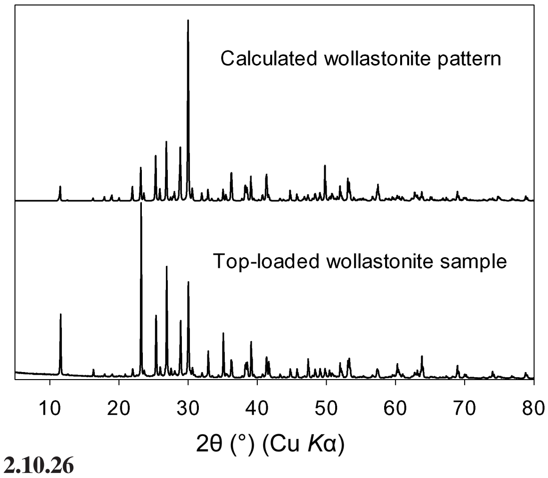

Figure 2.10.26
Effect of preferential orientation on data from top-loaded wollastonite compared with the calculated pattern from the literature wollastonite-1A structure (Ohashi, 1984).

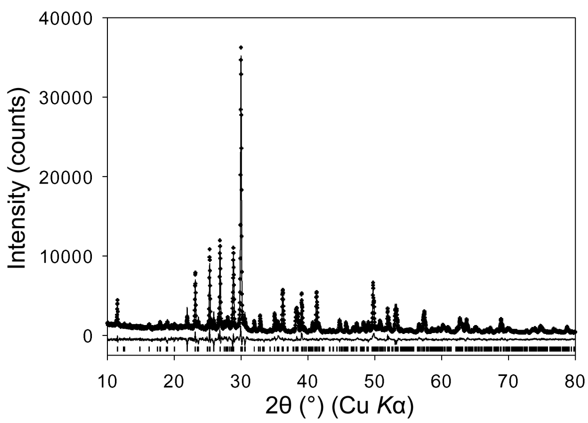

Figure 2.10.27
Rietveld refinement fit to the literature wollastonite-1A structure (Ohashi, 1984) with data from a 0.3 mm capillary with no orientation corrections.

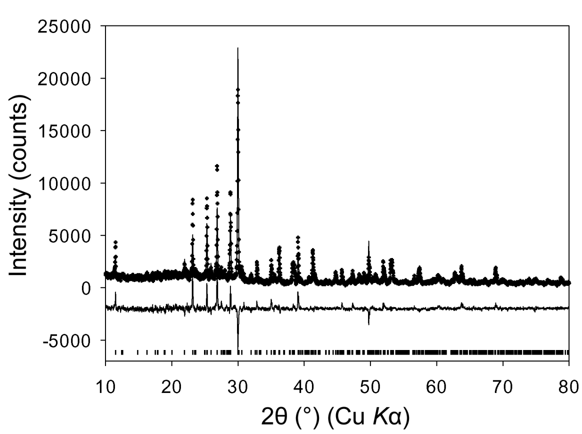

Figure 2.10.28
Rietveld refinement fit to the literature wollastonite-1A structure (Ohashi, 1984) with data from a 0.2 mm capillary with no orientation corrections.

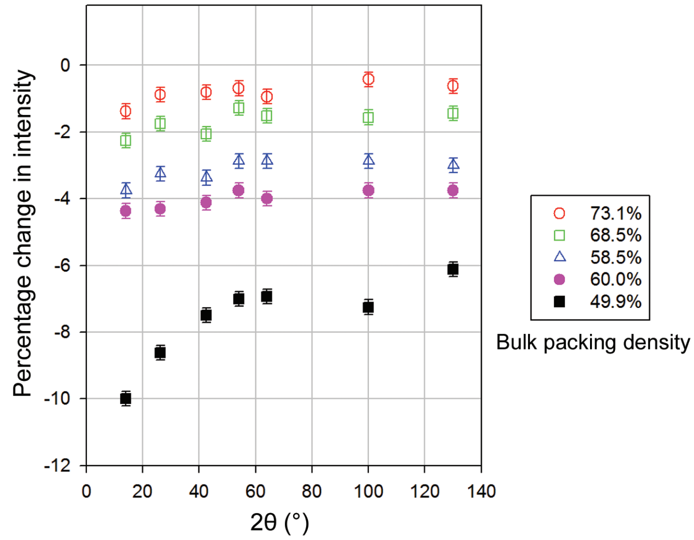

Figure 2.10.29
The effect of surface roughness on the intensity compared to that of a bulk copper specimen. Data from Suortti *et al.* (1972).

intact while filling the capillary (Fig. 2.10.23). Fig. 2.10.24 gives a summary of the effectiveness of the different sample-preparation techniques for this particular mica sample in terms of the ratio of the integrated intensities of the 001 and 200 reflections. The spray-dried sample with careful top loading can produce a pattern practically equivalent to the capillary data set.

Plates are not the only problematic morphology. Needle-shaped crystallites such as those exhibited by wollastonite (Fig. 2.10.25) and some organic compounds can also show significant problems when top-loaded. In fact, lath-like crystallites such as wollastonite can orient in two directions at the same time, so the behaviour can be more complicated than that of materials with plate-like morphology (see Figs 2.10.26, 2.10.27 and 2.10.28).

2.10.1.3. *Absorption (surface roughness), microabsorption and extinction*

Absorption, microabsorption and extinction effects all alter peak intensities, although particularly low absorption (*e.g.* from organics) can give rise to sample transparency in reflection geometry (as discussed in the section on the choice of sample mounting), where a peak shift and change in profiles can occur. Microabsorption and extinction solely affect the peak intensities.

Microabsorption (also known as absorption contrast) and extinction are effects that complicate quantitative phase analysis. They are both still related to size – particles in the case of microabsorption and crystallites in the case of extinction.

2.10.1.3.1. *Absorption (surface roughness)*

Absorption is an obvious issue when using capillaries in transmission (a convenient calculator is available on the 11-BM web site, http://11bm.xray.aps.anl.gov), but absorption can also affect data obtained in reflection using Bragg–Brentano geometry through the mechanism commonly described as 'surface roughness'. In essence, the increasing packing density with depth leads to lower intensities at low diffraction angles, leading to anomalously low or negative displacement parameters (much as absorption does in capillaries). There are two components to the effect (Fig. 2.10.29, Suortti, 1972). The constant decrease in intensity is generally incorporated into the refined scale factor. The angle-dependent portion becomes more significant as the packing density is reduced.

The effect is greatest with strongly absorbing materials analysed in reflection geometry, so care should be taken to produce a sample with a smooth surface and uniform density where possible. An example is provided by the patterns (Fig. 2.10.30) of a commercial cobalt silicate (which turned out to consist of a mixture of phases). A pattern from a slurry deposited on a zero-background cell – a technique useful for small samples, but which produces a rough surface – yielded significantly lower

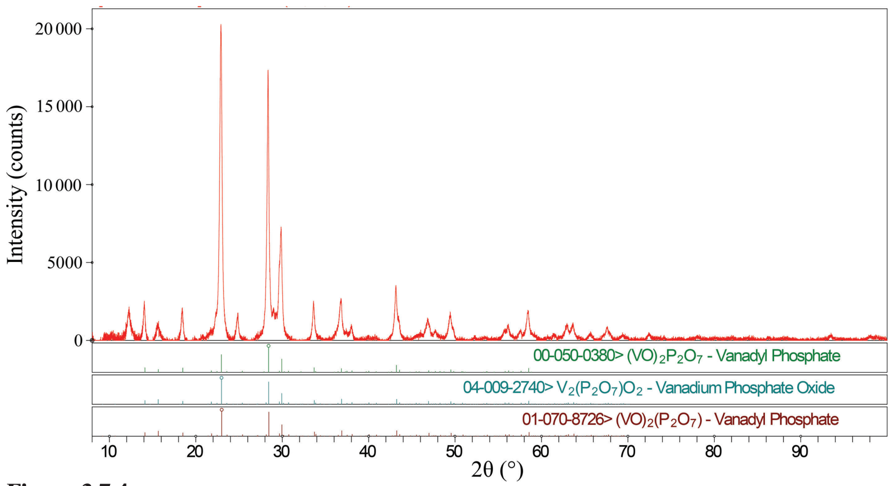

Figure 3.7.4
The results of applying a commercial search/match program (*Jade* 9.5; Materials Data, 2012) to the (background-subtracted, $K\alpha_2$-stripped) powder pattern of a butane-oxidation catalyst. The first three patterns in the hit list had equivalent figures of merit. The PDF entries 00-050-0380 and 04-009-2740 had Star quality marks and 04-009-2740 contained the atomic coordinates necessary for a Rietveld refinement. Additional peaks are apparent. The phases that give rise to them were identified using the native capabilities of the Powder Diffraction File.

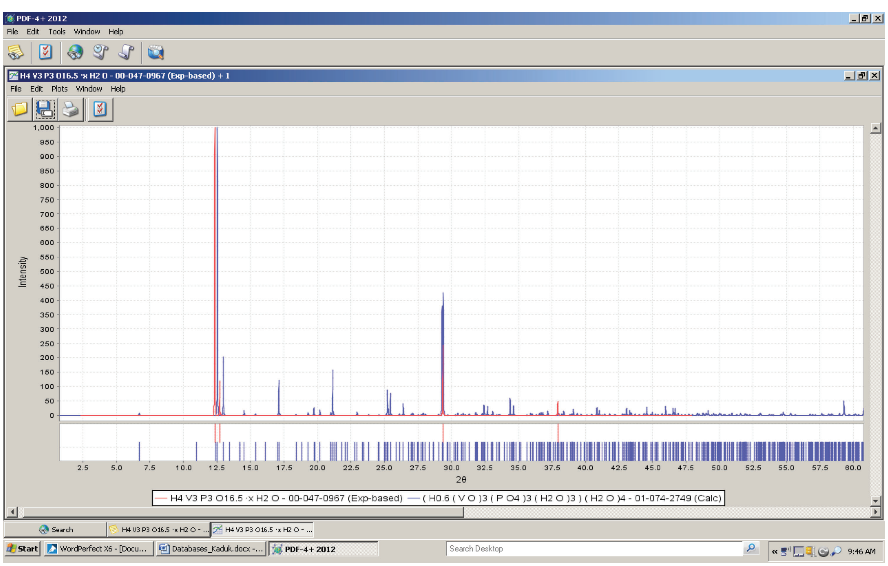

Figure 3.7.5
Comparison of the low-quality experimental PDF entry 00-047-0967 with the high-quality calculated pattern 01-074-2749 located by searching the experimental pattern against the rest of the PDF. The similarity in patterns and chemistry demonstrated that the two phases were the same and that the coordinates used to calculate entry 01-074-2749 could be used in a Rietveld refinement of a butane-oxidation catalyst.

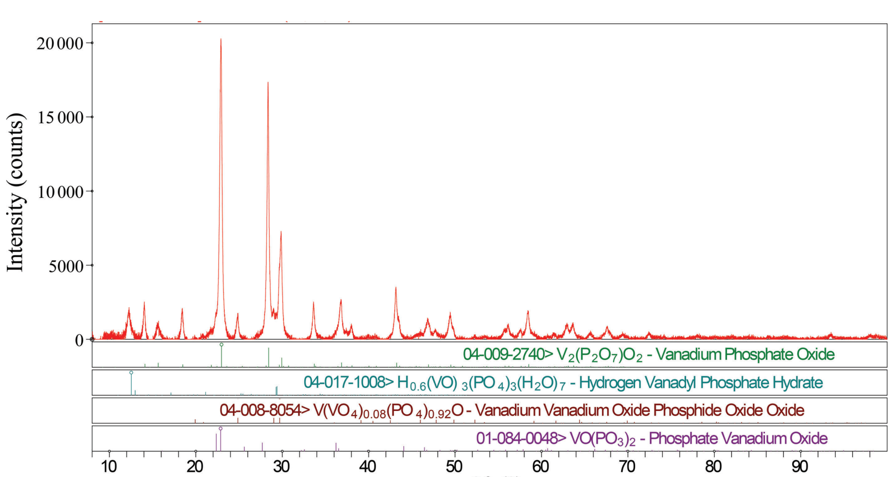

Figure 3.7.6
The four crystalline phases identified in a butane-oxidation catalyst.

3.7.2.4.4. *Isocracker sludge*

An isocracker is a refinery unit which simultaneously carries out cracking and isomerization reactions to produce more high-octane gasoline. A black deposit isolated from such a unit was surprisingly crystalline (Fig. 3.7.9; files NALK157.gsas, NALK157.raw and padv.prm). It was easy to identify small concentrations of elemental sulfur, pyrrhotite-4M (now called pyrrhotite-4C), haematite, lepidocrocite and dolomite, but the major peaks did not match well those of any entry in the PDF.

It seemed likely that a mineral-related phase would serve as a structural prototype for an apparently new phase, so two separate searches for mineral-related phases with one of their three strongest peaks in the *d*-spacing ranges 7.09 ± 0.03 and 5.57 ± 0.03 Å were combined. The two hits in the search list were both uranium minerals. These seemed unlikely in a refinery deposit(!). Widening the search ranges to 7.09 ± 0.10 and 5.57 ± 0.07 Å yielded rasvumite, KFe_2S_3 (PDF entry 00-033-1018), as the second entry in the hit list.

The fit to the major peaks in the deposit was reasonable, but there should not be any potassium in a refinery deposit and none was detected in a bulk chemical analysis. When the jar containing the deposit was opened, it smelled strongly of ammonia. Ammonium and potassium ions are about the same size and often form isostructural compounds. The infrared spectrum of the deposit was dominated by bands of ammonium ions.

The potassium in the structure of rasvumite (PDF entry 01-083-1322, used as a reference) was replaced by nitrogen. Analysis of potential hydrogen-bonding interactions yielded approximate hydrogen positions in the ammonium ion. These positions were refined using a density-functional geometry optimization. This model yielded a satisfactory Rietveld refinement (Fig. 3.7.10) and the quantitative analysis 45.7 (2) wt% $(NH_4)Fe_2S_3$, 12.8 (4) wt% S_8, 22.0 (6) wt% lepidocrocite (γ-FeOOH), 5.5 (5) wt% haematite (α-Fe_2O_3), 6.6 (3) wt% pyrrhotite-4C (Fe_7S_8) and 6.6 (3) wt% dolomite [$CaMg(CO_3)_2$; limestone environmental dust]. The powder pattern and crystal structure of $(NH_4)Fe_2S_3$ are now included in the PDF as entry 00-055-0533.

3.7.2.4.5. *Amoxicillin*

The amoxicillin powder from a commercial antibiotic capsule was highly crystalline. Its powder pattern (files kadu918.gsas, KADU918.raw, d8v3.prm and KADU921.rd) was matched well by the PDF entries 00-039-1832 and 00-033-1528 for amoxicillin trihydrate, but there was an additional peak at a *d*-spacing of 16.47 Å (5.37° 2θ). With such a low-angle peak, it seemed prudent to measure the pattern again

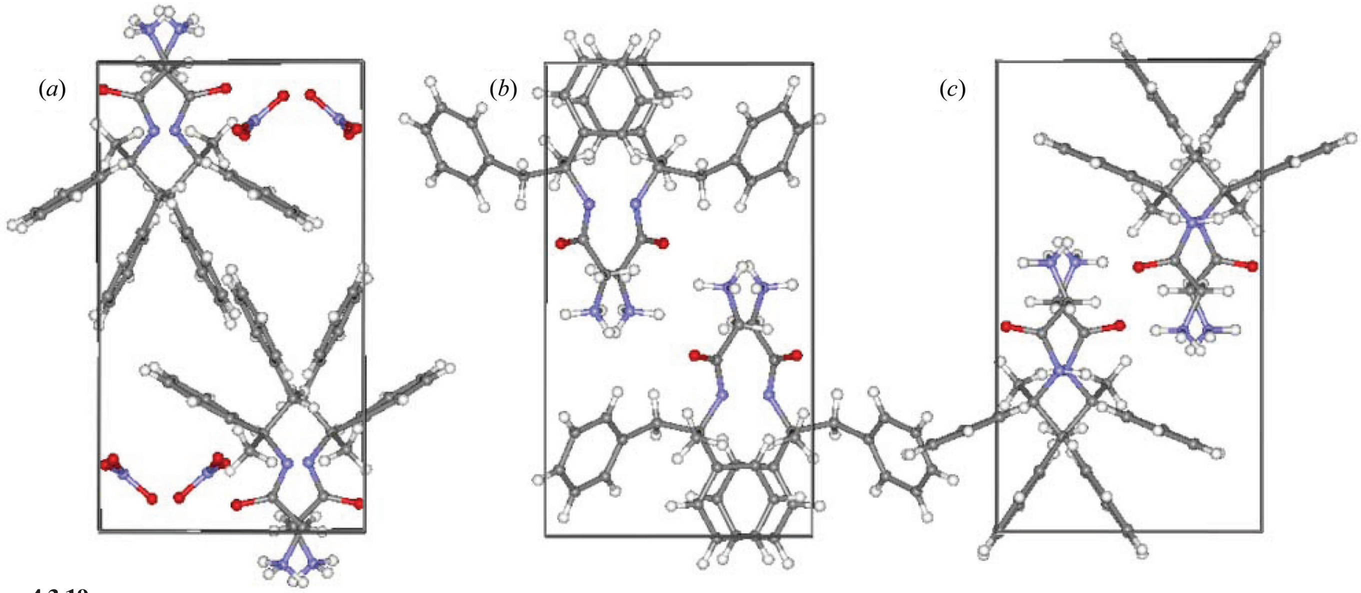

Figure 4.3.19
(*a*) The correct crystal structure of remacemide nitrate. (*b*) The best structure determination using a least-squares analysis to compare observed and calculated diffraction data with only the remacemide ion used in the structural model. Note that although the structural arrangement is completely incorrect, it is clear that the solution has resulted in an optimal correlation of observed and calculated electron density. Note in particular that the phenyl group maps closely onto the scattering density associated with the nitrate ion. (*c*) The best structure determination using a maximum-likelihood analysis to compare observed and calculated diffraction data with only the remacemide ion used in the structural model. The structure illustrated in (*c*) is enantioimetrically related to correct solution shown in (*a*). The agreement between the remacemide molecular position, orientation and conformation in (*a*) and (*c*) is as close as obtained in a standard least-squares analysis with the nitrate ion included.

implementation of simulated annealing in *DASH*, the HMC approach is a factor of 2 more successful in locating the global minimum over a series of 20 repeat runs. From a comparison of Figs. 4.3.15 and 4.3.18, it is evident that the hybrid Monte Carlo algorithm is also significantly more efficient, requiring on average an order of magnitude fewer χ^2 evaluations.

4.3.6. Using maximum-likelihood techniques to tackle incomplete structural models

4.3.6.1. *Introduction*

Solving crystal structures from powder-diffraction data is a significantly more difficult and less straightforward procedure than its single-crystal counterpart because of the loss of information associated with compressing the three-dimensional reciprocal lattice on to the one dimension of a powder-diffraction pattern with the corresponding inevitable overlap of Bragg reflections. The situation can be ameliorated and Bragg-peak intensities more easily extracted by explicitly using texture or methods such as differential thermal expansion (Brunelli *et al.*, 2003). However, discussion of these experimental methods is beyond the scope of this chapter. The incorporation of additional chemical information directly into the structure-solution process using both databases and complementary experimental techniques is discussed in Chapter 4.4. This section discusses the reverse situation, where there is a lack of chemical information, and highlights the effectiveness of maximum-likelihood methods.

4.3.6.2. *Working with incomplete structural models: maximum-likelihood methods*

In the previous section, the use of additional information to facilitate real-space structure solution was discussed. Specifically, constraining molecular conformation, through the active use of torsion-angle distributions derived from the Cambridge Structural Database and the intramolecular distance restraints derived from solid-state NMR measurements, was shown to accelerate structure solution and extend the range of complexity of structures that may be solved using real-space structure-determination techniques (Middleton *et al.*, 2002).

In this section, a complementary strategy is discussed where not all the structure is initially determined. Consider the case of a co-crystal or salt compound where there is more than one type of molecule in the crystal structure. It is possible, through the use of maximum-likelihood techniques, to account for and effectively ignore a significant structural component and yet determine precisely the location of all of the rest of the crystal structure. Take the specific case of the anti-convulsant agent remacemide nitrate ($C_{17}H_{21}N_2O^+ \cdot NO_3^-$). Markvardsen *et al.* (2002) showed that, although the nitrate group accounts for ~18% of the X-ray scattering, a real-space structure solution, based not on a conventional least-squares but on a maximum-likelihood optimization between observed and calculated diffraction data, yielded the correct location, orientation and torsion angles of the remacemide ion without any attempt to locate the nitrate ion; see Fig. 4.3.19.

The maximum-likelihood method is perhaps best explained by specific reference to this crystal structure. The remacemide and nitrate ions will be denoted as the fragment and blur, respectively, for the purposes of the discussion. Given that the objective of the maximum-likelihood approach is to determine only the remacemide fragment, the *a priori* presumption is that the scattering contribution of the blur is randomly distributed throughout the unit cell. In reciprocal-space terms, this means that the calculated structure factors are no longer a set of numbers but are instead represented by a multidimensional Gaussian distribution with a width that is determined by the magnitude of the random scattering associated with the blur. As a consequence, the scattering density of the nitrate ion is actively considered in structure-factor representation, even though its position is explicitly unknown. With a large unknown component, the Gaussian broadening will be large and the

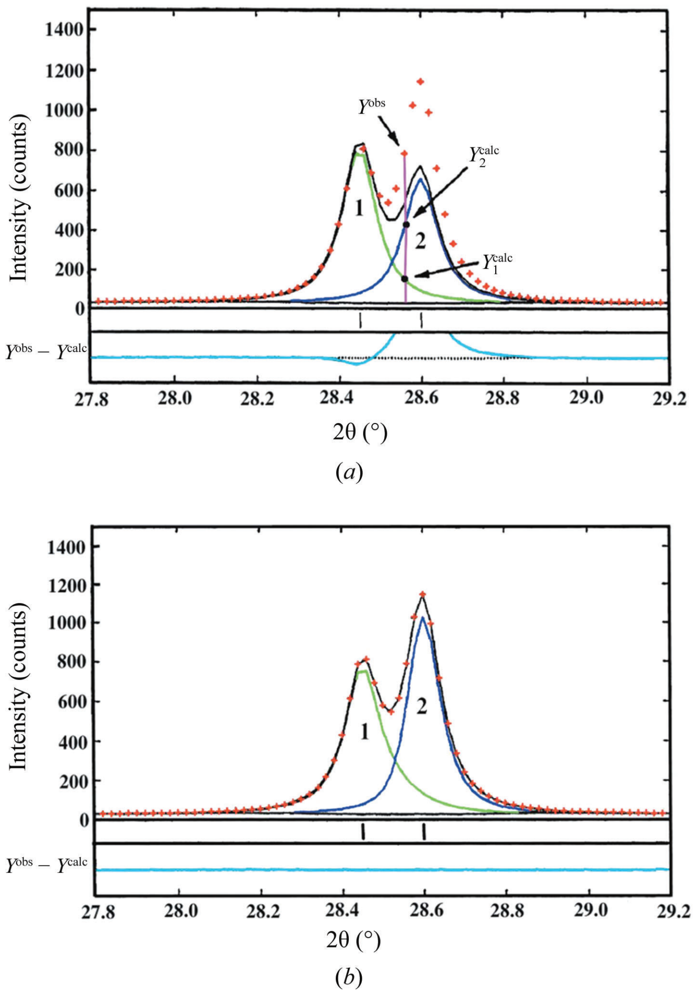

Figure 4.8.5
Observed intensity (points) as a function of the scattering angle, together with lines representing (*a*) the calculated intensity of the Rietveld refinement and (*b*) the intensities after decomposition according to equation (4.8.22) (from Takata, 2008).

uncertainties can be avoided by the use of so-called G constraints based on the integrated intensities of groups of overlapping reflections (Sakata *et al.*, 1990). G constraints can be easily incorporated into the Sakata–Sato algorithm, and are thus actively used in this algorithm.

G constraints are based on N_G groups of overlapping reflections. Group i has contributions of N_G^i reflections, resulting in a 'group amplitude' G^i equal to the square root of the integrated intensity and related to the structure-factor amplitudes through

$$G^i = \left[\sum_{j=1}^{N_G^i}\left(\frac{m_j}{\sum m_j}\left|F(\mathbf{H}_j)\right|^2\right)\right]^{1/2}, \qquad (4.8.23)$$

where m_j is the point-group multiplicity of reflection j. The summation runs over the symmetry-independent structure factors contributing to group i. The standard uncertainty of the group amplitude G_i follows as

$$\sigma(G^i) = \frac{1}{G^i}\left[\sum_{j=1}^{N_G^i}\left(\frac{m_j}{\sum m_j}\left|F(\mathbf{H}_j)\right|(\mathbf{H}_j)\right)^2\right]^{1/2}. \qquad (4.8.24)$$

The group amplitudes can be used in the G constraint in a similar way to the F constraint [equation (4.8.10)]:

$$C_G = -\chi^2_{\rm aim}(G) + \frac{1}{N_G}\sum_{i=1}^{N_G} w_i\left(\frac{G^i_{\rm obs} - G^i_{\rm MEM}}{\sigma\left(G^i_{\rm obs}\right)}\right)^2 = 0, \qquad (4.8.25)$$

where $G^i_{\rm obs}$ and $\sigma(G^i_{\rm obs})$ are the group amplitude and standard uncertainty as obtained from the experiment, respectively, and $G^i_{\rm MEM}$ is computed from $F_{\rm MEM}(\mathbf{H}_j)$ (Section 4.8.4) according to equation (4.8.23).

G constraints can be introduced into the MEM with aid of an additional Lagrange multiplier λ_G (see Section 4.8.4):

$$L = S - \lambda_N C_N - \lambda_F C_F - \lambda_G C_G. \qquad (4.8.26)$$

Experience has shown that a certain fraction of reflections must be available as F constraints in order for the MEM to converge to the correct electron-density distribution. Since the ratio of λ_F and λ_G is not known *a priori*, applications have used a single constraint with a single Lagrange multiplier λ_{FG} according to

$$L = S - \lambda_N C_N - \lambda_{FG} C_{FG} \qquad (4.8.27)$$

with the combined F and G constraint

$$\begin{aligned} C_{FG} = &-\chi^2_{\rm aim} + \frac{1}{N_{\rm all}}\sum_{i=1}^{N_F} w_i\left(\frac{\left|F_{\rm obs}(\mathbf{H}_i) - F_{\rm MEM}(\mathbf{H}_i)\right|}{\sigma(\mathbf{H}_i)}\right)^2 \\ &+ \frac{1}{N_{\rm all}}\sum_{i=1}^{N_G} w_i\left(\frac{G^i_{\rm obs} - G^i_{\rm MEM}}{\sigma\left(G^i_{\rm obs}\right)}\right)^2 = 0, \end{aligned} \qquad (4.8.28)$$

where $N_{\rm all} = N_F + N_G$ (Palatinus, 2003).

The formal solution of the MaxEnt equations then becomes [*cf.* equation (4.8.17)]

$$\begin{aligned} \rho_i = &\frac{N_{\rm el}N_{\rm pix}}{V_{\rm UC}}\rho_i^{\rm prior}\exp\left[-\lambda_{FG}\left(\frac{\partial C_F}{\partial \rho_i} + \frac{\partial C_G}{\partial \rho_i}\right)\right] \\ &\times\left\{\sum_{i=1}^{N_{\rm pix}}\rho_i^{\rm prior}\exp\left[-\lambda_{FG}\left(\frac{\partial C_F}{\partial \rho_i} + \frac{\partial C_G}{\partial \rho_i}\right)\right]\right\}^{-1}. \end{aligned} \qquad (4.8.29)$$

The implementation of G constraints in the Sakata–Sato algorithm is straightforward except for the computation of the derivative of the combined constraint, which is slightly more complicated than the calculation of the derivative of the F constraint.

4.8.6.2. *Constraints using 'partly phased' reflections for anomalous-scattering X-ray powder diffraction*

X-ray anomalous scattering from powders can be used for *ab initio* structure determination if at least two different data sets are available: one measured with a wavelength near the absorption edge of a chemical element contained in the sample and another measured with a wavelength far from the absorption edge. The corresponding Patterson map allows the localization of the resonant-scattering atoms. The phases of the resolved structure factors of centrosymmetric structures can be derived from this experiment. For noncentrosymmetric structures, two values remain for the phase φ_i of each reflection i. They can be written as $\varphi_i = \varphi_{0i} \pm \Delta_i$, where φ_{0i} and Δ_i are obtained from the experiment. This limited information from anomalous-scattering X-ray powder diffraction can be used in the MEM through the so-called A constraints for partly phased reflections (Burger & Prandl, 1999). Defining $A'^i = |F|\cos(\Delta_i)$ and $B'^i = |F||\sin(\Delta_i)|$, the A constraint is

$$t_{\text{per}} = t_A + t_B. \tag{5.4.71}$$

Such superlattices are fabricated for applications as so-called Bragg mirrors in light-emitting devices or as X-ray mirrors. The X-ray reflectivity curves of such multilayers have various characteristic features that are illustrated for the example of an X-ray mirror system in Fig. 5.4.22. The figure also displays the reflectograms of a 10 × (6 nm TiO_2/6 nm C) superlattice on an Si substrate that was again calculated using *RCRefSim* (Zaumseil, 2005). As for the single-layer system, a modified Bragg equation (5.4.53) may be derived describing the occurrence of the superlattice peaks by inserting t_{per} instead of t,

$$\theta_m^2 = \langle\theta_c\rangle^2 + m^2\left(\frac{\lambda}{2t_{\text{per}}}\right)^2, \tag{5.4.72}$$

where $\langle\theta_c\rangle$ is the average critical angle of the total superlattice. The thickness values for each individual layer A and B and the interface roughness σ_{AB} and σ_{BA} can be determined by fitting with the matrix formalism. The figure displays three different simulations with varying interface roughnesses. The difference between the large fringes is accounted for by (5.4.72), while the small fringing scales with the total thickness of the layer system, *i.e.* $1/(Nt_{\text{per}})$. Ideally, there are $N - 2$ small fringes between two adjacent superlattice peaks. It can be realized from the figure that for certain combinations of σ_{AB} and σ_{BA} every second maximum may vanish. This effect may be observed in superlattices having $t_A = t_B$ and is due to the destructive interference from X-ray beams reflected at the AB and BA interfaces.

Superlattices with large differences in electron density between individual layers can be used as X-ray mirrors. Typical material combinations are Mo/Si, V/C or La/B_4C and other systems with substantial ρ_e contrast. XRR also provides a sensitive tool for studying the surface oxidation of metals and other materials that are sensitive to surface oxidation. In fact, in his seminal study Parrat investigated a thin copper film on glass, where reliable agreement between the measured and simulated reflectivity could only be achieved by introducing a 15 nm-thin surface-oxide layer into the model (Parratt, 1954). The possibility that there may be an oxide layer on the top of a thin-film or multilayer system should routinely be considered when fitting measured reflectivity curves. Surface chemical reactions may also be studied by XRR.

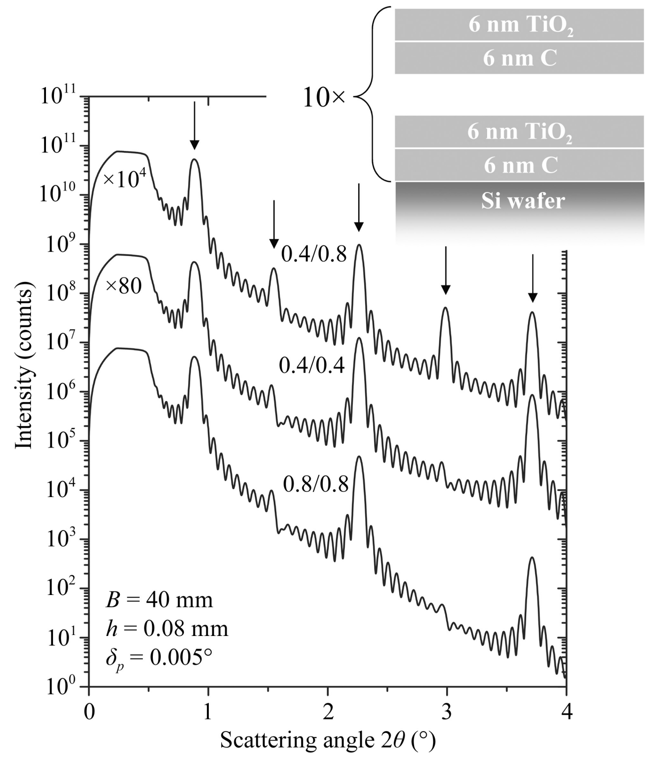

Figure 5.4.22
Simulation of X-ray reflectivity of a (TiO_2/C) superlattice on an Si wafer. The numbers above the pattern give the roughnesses of the TiO_2 and C layers, respectively, in nanometres. The substrate roughness was set to a constant 0.4 nm. Superlattice peaks are indicated by arrows.

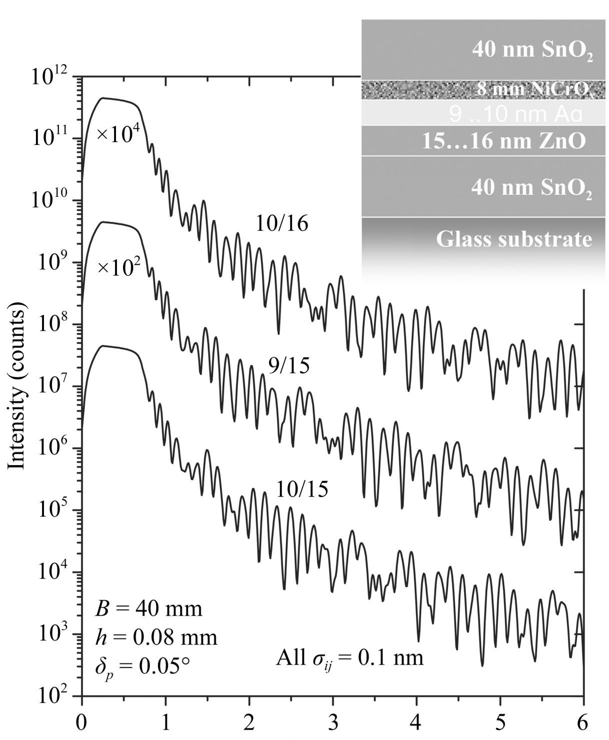

Figure 5.4.21
Simulated X-ray reflectivity patterns of barrier coating SnO/NiCrO$_x$/Ag/ZnO/SnO on glass recorded with Cu $K\alpha$ radiation. The numbers above each pattern indicate the thicknesses of the Ag and ZnO layers, respectively, in nanometres. Other thicknesses were kept constant.

5.4.7. Grazing-incidence X-ray scattering (GIXS)

In a GIXS experiment, a primary beam with momentum $\mathbf{K}_0$ impinges on the sample at a very small incidence angle, as in XRR. Again, the elastically scattered intensity with momentum vector $\mathbf{K}$, $|\mathbf{K}| = |\mathbf{K}_0| = 2\pi/\lambda$, is measured in a reflective configuration, but it is not the specular reflection alone that is measured by a point detector. Instead, the intensity in GIXS is collected by a two-dimensional detector screen, allowing scattering events for which the scattering vector $\mathbf{Q} = \mathbf{K} - \mathbf{K}_0$ deviates from the substrate normal to also be recorded. The incidence angle between the primary (scattered) beam and the substrate surface is generally denoted by α_i (α_f), while the azimuth of the scattered beam is indicated by $2\theta_f$. The two-dimensional intensity map is then given as a function of momentum-transfer coordinates Q_y and Q_z according to

$$\begin{aligned} Q_y &= \frac{2\pi}{\lambda}\sin\theta\cos\alpha_f\sin 2\theta_f,\\ Q_z &= \frac{2\pi}{\lambda}\sin\theta(\sin\alpha_i + \sin\alpha_f), \end{aligned} \tag{5.4.73}$$

where the projection of $\mathbf{K}_0$ to the sample surface is assumed to define the x axis. The method is often used with small scattering angles, and in this case is denoted as GISAXS. The analysis of

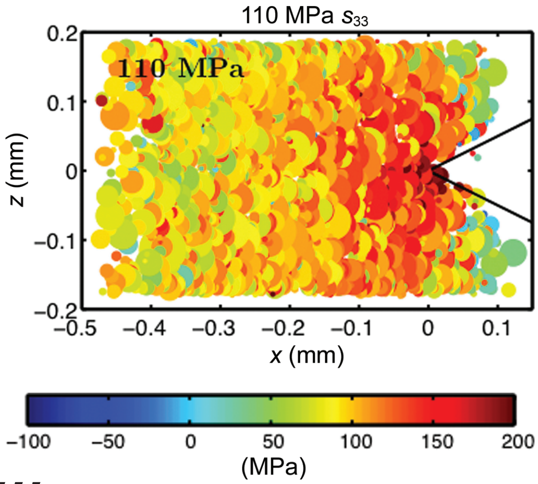

Figure 5.5.5
Stress map of 1750 grains around a notch in an Mg AZ321 sample during tensile deformation. Shown is the axial stress in each grain at an external load of 110 MPa colour coded according to the colour bar at the bottom. The figure represents a 2D projection of the 3D map. The diameters of the spheres represent the grain sizes. Reprinted from Oddershede *et al.* (2012), with permission from Elsevier.

$\simeq 10^{-4}$ and grain orientations to 0.5° precision (Margulies *et al.*, 2002; Martins *et al.*, 2004; Oddershede *et al.*, 2012; Bernier *et al.*, 2011). These properties imply that the method is well adapted to studies of grain rotations (*e.g.* Poulsen *et al.*, 2003). Furthermore, having determined the entire strain tensor for each grain, the corresponding stress tensor can be derived, using Hooke's law; see Section 5.5.10. Fig. 5.5.5 is an example of the application of such stress mapping. In practice this formalism is applicable up to 5–10% plastic deformation; at higher external loads the centre-of-mass algorithms tend to break down because of spot overlap.

5.5.8. 3D grain and orientation mapping

3DXRD microscopy and diffraction contrast tomography (DCT) enable relatively fast generation of large 3D grain maps and 3D orientation maps by use of tomographic reconstruction algorithms. The development of such algorithms is non-trivial, as the complexity in terms of the dimensionality and sheer size of the reconstruction space is much larger than for classical tomography. Another difference is that in 3DXRD and DCT the number of useful projections is given by the number of observable reflections and as such is intrinsically limited (Poulsen, 2004).

In the most general case, some or all of the grains may be smaller than the voxel size and as such the relevant representation is in terms of associating an orientation distribution function, ODF, with each voxel. This implies operating in a numerically very large six-dimensional solution space. Reconstruction algorithms for this case are not routinely available. In practice, focus has been on vector-field reconstructions, where each voxel is associated with one and only one orientation. However, even with this constraint, further simplifications may be required for computational reasons.

An important simplification is the case where the grains are both large in comparison to the voxel size and 'undeformed'; that is, the orientation spread within each grain is negligible. In this case the spatial and angular degrees of freedom are separate, and one may effectively reconstruct *grain maps* rather than orientation maps. Mathematically speaking, the task at hand in this case is to determine the 3D boundary network with as high a precision as possible.

Furthermore, if the diffraction spots do not overlap, one may initially index the various grains, and then reconstruct the 3D morphology of individual grains independently. Powerful methods from the field of discrete tomography can then be applied, allowing for reconstructions even in the case of very few projections (Alpers *et al.*, 2006; Batenburg *et al.*, 2010). The first 3D grain maps were of this kind (Fu *et al.*, 2003).

Another simplification for reconstructing both grains and orientations is the use of a line beam, *cf.* Fig. 5.5.1. In this case, 3D maps are generated by stacking independent reconstructions from a set of layers.

At the time of writing, orientation maps comprising up to 20 000 grains have been obtained. The spatial resolution is of the order 1–5 µm. Using synchrotron sources, the data-acquisition time for a full 3D map is typically of the order of a few hours.

Below we outline two popular approaches for reconstruction.

5.5.8.1. *Approach 1: Grain-by-grain volumetric mapping*

In this approach it is assumed that the grains have negligible orientation gradients. First, the orientations and centres-of-mass of the grains are found, *cf.* Section 5.5.7. Then the 3D shape of each grain is reconstructed. Owing to experimental uncertainties the shapes of the grains will not form a perfect 3D space-filling map, so the last step in the procedure is typically an optimization of the grain-boundary position based on standard image-analysis techniques such as smoothing or erosion/dilation. In practice, the presence of voids can be a concern when the aim is to reach a detailed description of boundary curvatures and triple-junction geometry.

Diffraction contrast tomography (*e.g.* Johnson *et al.*, 2008; Ludwig *et al.*, 2008; King *et al.*, 2008) is performed in this way, as are standard 3DXRD microscopy experiments. As an example of such work, Fig. 5.5.6 shows a grain map of a β-Ti sample reconstructed by the DCT algorithm.

5.5.8.2. *Approach 2: Orientation mapping by Monte Carlo optimization*

Classical transform algorithms are not well suited to handling vector-field reconstructions. Focus has therefore been on Monte Carlo based optimization routines. An example is the forward-

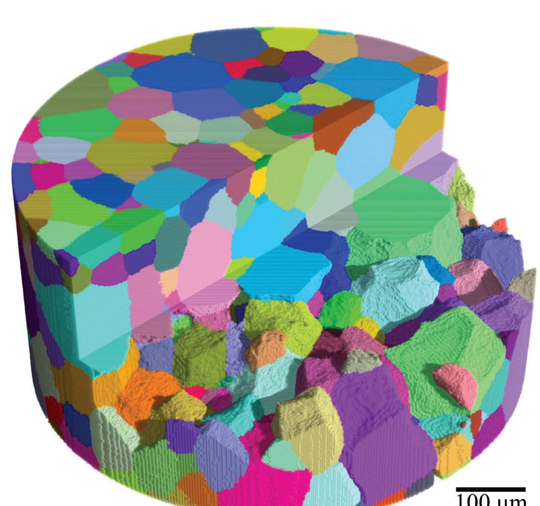

Figure 5.5.6
Rendition of the 3D grain structure in a cylindrical β-Ti specimen containing 1008 grains, as obtained by the DCT algorithm. From Ludwig *et al.* (2008).

citly, *PDFgetX2* (Qiu *et al.*, 2004). This approach does not result in a PDF on an absolute scale, which is generally not a problem when modelling the data since an overall scale factor can be applied to the calculated PDF. In practice, our experience is that data sets collected at the same time (for example, a temperature series) and processed using *PDFgetX3* all appear with the same scale factor and features such as peak heights can be compared with each other even without modelling.

5.7.5. Extracting structural information

5.7.5.1. *Obtaining the PDF from a model*

Assume that we have a model for our sample that consists of a set of N atoms at positions $\mathbf{r}_i$ with respect to some origin. The model is built up as described in Section 5.7.2.2.

If we consider a crystalline single-element material, for example nickel, a typical neutron-sized sample contains in the vicinity of 10^{20} or more atoms. To properly calculate $R(r)$ we would therefore need to carry out a double sum over this many atoms, which is completely impractical. However, in practice accurate PDFs can be calculated from many fewer (and a practically small number of) atoms. First, we are generally only interested in calculating $R(r)$ over a relatively narrow range of r, say 20 Å. In this case, we would still need to put the origin on each of the 10^{20} atoms in turn to accurately represent the sample, but each time the sum need only be taken over atoms that lie within 20 Å of the origin atom, a volume that contains only 10^2–10^3 atoms. Second, the material in question may be crystalline. In this case, the total sample is made up of many equivalent unit cells which are periodically repeated in space (although it should be noted that in real crystals, the ideal of every unit cell being

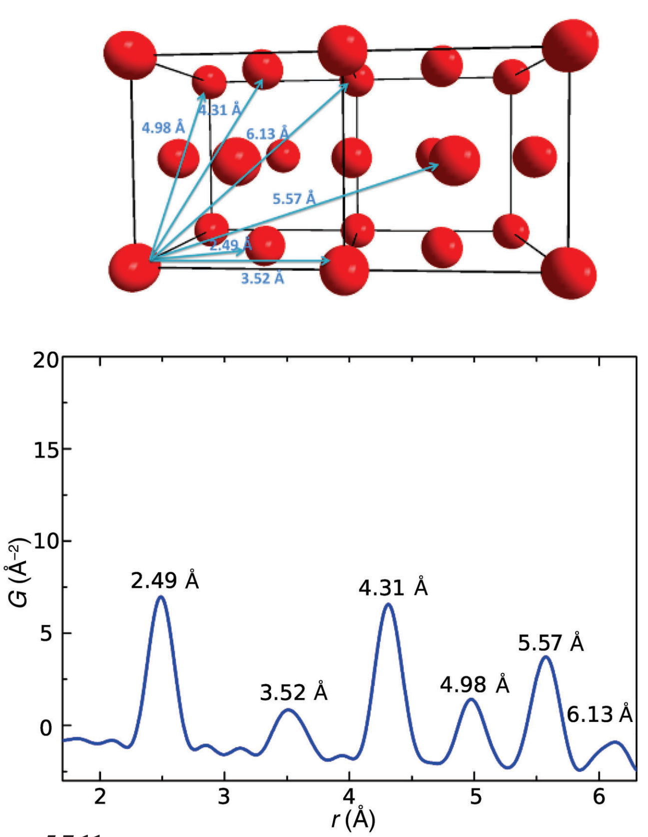

Figure 5.7.11
A schematic of the buildup of the PDF from the structural model for face-centred-cubic nickel. The top figure shows the bond distances of nearby atoms from a reference Ni atom at the corner. Its corresponding PDF is shown below.

identical may not hold well). In this favourable situation we need only place the origin on each atom in the unit cell, since the equivalent atom in all the other unit cells has exactly the same atomic environment. This is now a computationally tractable problem: a double sum where the first sum is taken over the atoms in the unit cell (typically <100) and the second sum over all atoms within $r_{\max}$ of the origin atom, where $r_{\max}$ is the maximum extent over which the PDF is to be calculated. This is shown in Fig. 5.7.11.

Even in the case where the sample is nanocrystalline or amorphous, sufficient averaging over different possible configurations to replicate the measured PDF is in general possible with a much smaller number of atoms. For example, in typical big-box modelling approaches such as reverse Monte Carlo, boxes containing $\sim 10^4$ atoms are typical.

5.7.5.2. *PDFs from multi-element material*

When calculating the PDF from samples with multiple atomic species, we need an expression for the calculated radial distribution function expressed in terms of partial radial distribution functions between different atom types. In analogy to Section 5.7.2.6, when multiple elements are present in the sample we can write

$$\begin{aligned} R(r) &= \frac{1}{N\langle f\rangle^2} \sum_{i,j(i\neq j)} f_j^* f_i \delta(r - r_{i,j}) \\ &= \frac{1}{\langle f\rangle^2} \sum_{\alpha,\beta} \sum_{i\in\{\alpha\}, j\in\{\beta\}(i\neq j)} \frac{f_\alpha^* f_\beta}{N} \delta(r - r_{i,j}) \\ &= \sum_{\alpha,\beta} \frac{c_\alpha c_\beta f_\alpha^* f_\beta}{\langle f\rangle^2} \left(\sum_{a,b} \frac{1}{N c_\alpha c_\beta} \delta(r - r_{i,j}) \right) \\ &= \sum_{\alpha,\beta} \frac{c_\alpha c_\beta f_\alpha^* f_\beta}{\langle f\rangle^2} R_{\alpha\beta}, \end{aligned} \tag{5.7.63}$$

which serves to define

$$R_{\alpha\beta} = \frac{1}{N c_\alpha c_\beta} \sum_{a,b} \delta(r - r_{i,j}). \tag{5.7.64}$$

5.7.5.3. *Model-independent information from the PDF*

It is clear from this description that the PDF is a heavily averaged representation of the structure. First, directional information is lost. Second, it is a linear superposition of the local environments of many atoms. How can such a function contain any useful information at all? The reason is that, especially on very short length scales, the possible environments of particular atoms are very limited. In nickel, for example, all the atoms have the same number of neighbours (12) at the same nearest-neighbour distance, $r_{\rm nn}$ = 2.49 Å (Wyckoff, 1967). There is no intensity in $R(r)$ for $r < r_{\rm nn}$ and a sharp peak at $r_{\rm nn}$. This behaviour is very general and true even in atomically disordered systems such as glasses, liquids and gases. In such systems the second and higher neighbour distances are generally less well defined and the PDF peaks are broader. However, in crystals, because of the long-range order of the structure, all neighbours at all lengths are well defined and give rise to sharp PDF peaks (Levashov *et al.*, 2005). The position of these peaks directly gives the separations of pairs of atoms in the structure. If data are measured with high enough $Q_{\max}$, finding the position of a peak maximum will give the distance separating a pair of atoms in the material. If the

Table 6.1.1
Software for powder diffraction

Program	Description	Function(s)	Reference(s)	URL or other source	Availability
ACerS–NIST Phase Equilibria Diagrams Database	Phase-equilibria diagrams	Database	ACerS–NIST Phase Equilibria Diagrams Database (2013)		Commercial
ADM	Software suite including device control, pattern evaluation, qualitative and quantitative phase analysis, indexing, lattice-parameter refinement, crystal-size evaluation, microstress analysis, profile analysis and pattern simulation	Phase analysis, indexing, lattice-parameter refinement, crystal size, stress, profile analysis, pattern simulation		http://www.RMSKempten.de/	Commercial
American Mineralogist Crystal Structure Database (AMCSD)	Online database that includes every structure published in *The American Mineralogist*, *The Canadian Mineralogist*, *European Journal of Mineralogy* and *Physics and Chemistry of Minerals*, as well as selected data sets from other journals	Minerals, database	Downs & Hall-Wallace (2003)	http://rruff.geo.arizona.edu/AMSamcsd.php	Free to use
ANAELU	Computer-based tools for inferring single-crystal structures and fibre textures from two-dimensional diffraction diagrams	Modelling, glasses	Fuentes-Montero *et al.* (2011)	http://www.esrf.eu/computing/scientific/ANAELU/Anelu_Page.htm	Free
ARITVE	Modelling of glass structures using the Rietveld method	Modelling, glasses	Le Bail (1995, 2000)	http://sdpd.univ-lemans.fr/aritve.html	Free
ATOMS	Structure visualization. Part of the *SHAPE* software package	Structure visualization	Shape Software, 521 Hidden Valley Road, Kingsport, TN 37663, USA	http://www.shapesoftware.com/	Commercial
AUTOFP	GUI for highly automated Rietveld refinement using an expert system algorithm based on *FULLPROF*	Rietveld refinement	Cui *et al.* (2015)	http://pmedia.shu.edu.cn/autofp	Free
AUTOX	Autoindexing multiphase samples; included with *VMRIA*	Indexing	Zlokazov (1995); Bergmann *et al.* (2004)	http://www.ccp14.ac.uk/ccp/web-mirrors/vmria	Free
AXES	Program for X-ray powder diffraction data evaluation, specially designed for peak-shape analysis and data preparation for Rietveld refinement in connection with *FULLPROF*	Data conversion, peak-shape analysis	Mändar *et al.* (1996)	http://www.ccp14.ac.uk/ccp/web-mirrors/axes/~hugo/axes/	Free for academic use
AXES-20B	Estimation of crystal size and shape. Links to a wide range of programs and includes a range of data-processing and display functions	Phase identification, data conversion, structure visualization, peak location, peak profiling, indexing	Mändar & Vajakas (1998); Mändar *et al.* (1999)	http://www.ccp14.ac.uk/ccp/web-mirrors/axes/	Free
Balls&Sticks	Structure visualization and animation	Structure visualization	Ozawa & Kang (2004)	http://www.toycrate.org/	Free
BALSAC	Construction, visualization and interactive analysis of crystal lattices	Structure visualization	K. Hermann, Fritz-Haber-Institut der MPG, Berlin, Germany	http://www.fhi-berlin.mpg.de/~hermann/Balsac/	Free
BEARTEX	Texture analysis in polycrystalline materials	Texture analysis	Wenk *et al.* (1998)	http://eps.berkeley.edu/~wenk/TexturePage/beartex.htm	Free

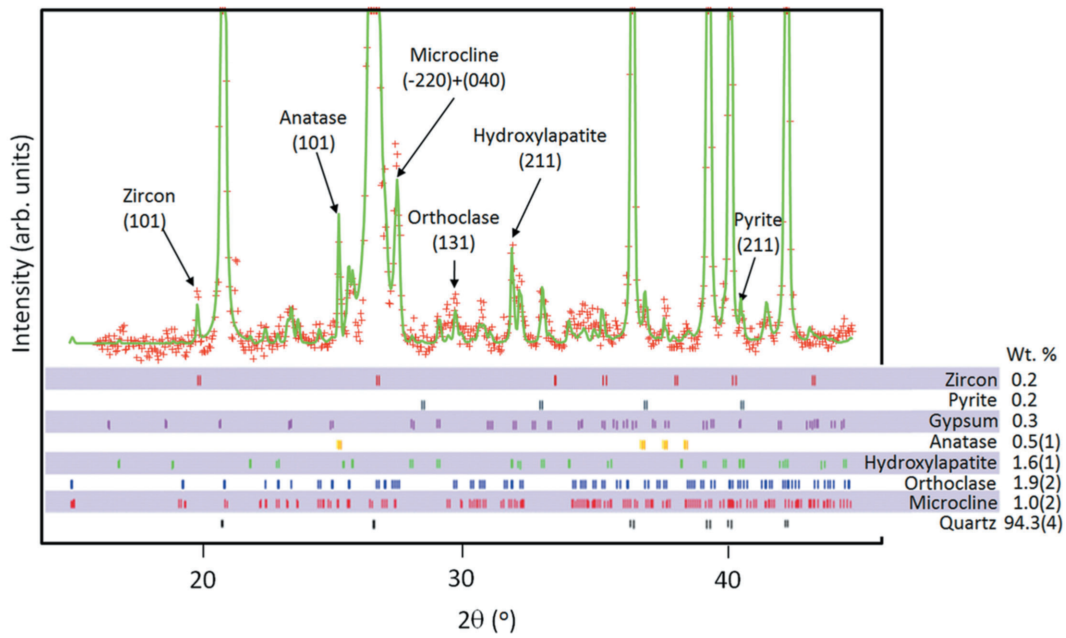

Figure 7.3.1
Multi-phase Rietveld refinement of a borehole specimen. The line shows the calculated pattern. Raw data points are shown as + symbols. Individual peaks for the trace phases are highlighted by arrows. Off-scale peaks are from quartz. Reflection tick marks for each phase are shown below the pattern. Quantitative weight % values for the phases are listed on the lower right of the plot. See Rodriguez *et al.* (2012). Copyright (2012) JCPDS – International Centre for Diffraction Data. Reproduced with permission.

release initiated upon conversion of the low-temperature γ-$Ca(BH_4)_2$ phase to the high temperature β-$Ca(BH_4)_2$ phase. Synchrotron sources also have the advantage of a tunable X-ray wavelength and are therefore not restricted to a fixed wavelength as dictated by the anode of a standard sealed-tube source. In this regard, synchrotron sources are often employed for atomic pair distribution function (PDF) analysis. This is because synchrotron sources can easily generate the hard X-ray wavelengths (*e.g.* <0.5 Å) that are necessary to achieve high momentum-transfer values (*i.e.* $Q_{max} > 20$ Å^{-1}) in measured data sets (see Chupas *et al.*, 2003). PDF data are useful for characterizing nearest-neighbour distances between atomic species in a structure and can be beneficial for both crystalline and non-crystalline compounds. Chupas *et al.* (2007) demonstrated the use of synchrotron radiation to detect the presence of H_2 in $Mn_3[Co(CN)_6]_2{\cdot}3H_2$ by differential PDF analysis. This approach revealed how the H_2 molecules are bound within the porous framework, resulting in a more detailed understanding of how H_2 is stored and recovered from the material. While access to synchrotron facilities is often limited, well designed experiments can lead to significant knowledge of a material's behaviour. Chapter 2.2 in this volume is dedicated to synchrotron radiation and the reader is referred to that chapter for further details.

7.3.4. Wind

One of the critical aspects of green technologies such as wind and solar is the intermittent nature of the harvested energy, which dictates the necessity for energy storage. Wind farms have been employing a clever strategy for power storage through the use of compressed air energy storage (CAES), as outlined by Cavallo (2007). This method employs the use of underground caverns (man-made or naturally occurring). When the wind is active at a time of low power demand, a wind farm may choose to transfer power to an air compressor that pumps air into a cavern, thereby storing the energy in the form of pressure. The energy can be converted back to electricity by releasing the air pressure through a turbine. Careful characterization of cavern geology is important, especially with regard to the materials present in the access boreholes that are drilled deep into the ground to bridge the cavern to the surface (Rodriguez *et al.*, 2012). Quantitative characterization of the phases present as a function of depth is important information for assessing the impact of cyclic air pressure on the CAES station. Fig. 7.3.1 shows a Rietveld refinement for an eight-phase diffraction pattern obtained from a core-drill specimen. The identification of the phases was facilitated by employing X-ray fluorescence (XRF) for determination of the elemental composition (Rodriguez *et al.*, 2012). It is worth noting that the plot in Fig. 7.3.1 shows intensity for phases that are very close to the background level. The quartz peaks, which make up more than 90 wt% of the sample, go off-scale on the intensity axis. This allows the signals from the other minor or trace phases present to be seen more easily. One phase of critical importance for CAES functionality was FeS_2 (pyrite), because oxidation of this phase could alter the pH and mineralogy of the borehole. The phase analysis *via* Rietveld refinement revealed a very small weight fraction of pyrite at this borehole depth. In fact, the quantity was so small and confounded by peak overlap with other phases that its detection proved difficult without the supporting XRF analysis. Typical errors associated with phase quantification are in the 0.1 to 0.5 weight percent range, depending on the quality of the XRD data and the scattering behaviour of the quantified phase. This is one of the limitations of powder XRD. Detection and quantification of major, minor and trace phases *via* XRD analysis can give better insight into the functionality and possible issues that might impact CAES, a practical option for energy storage at large wind-farm facilities.

7.3.5. Solar

The challenge of solar technology is to efficiently convert photonic energy from sunlight into another form of energy, typically electricity. The solar cell is the quintessential building block of the industry, but materials science challenges still remain. The three best-known issues with photovoltaics are: (1) the influence of grain boundaries, (2) the electron affinity of

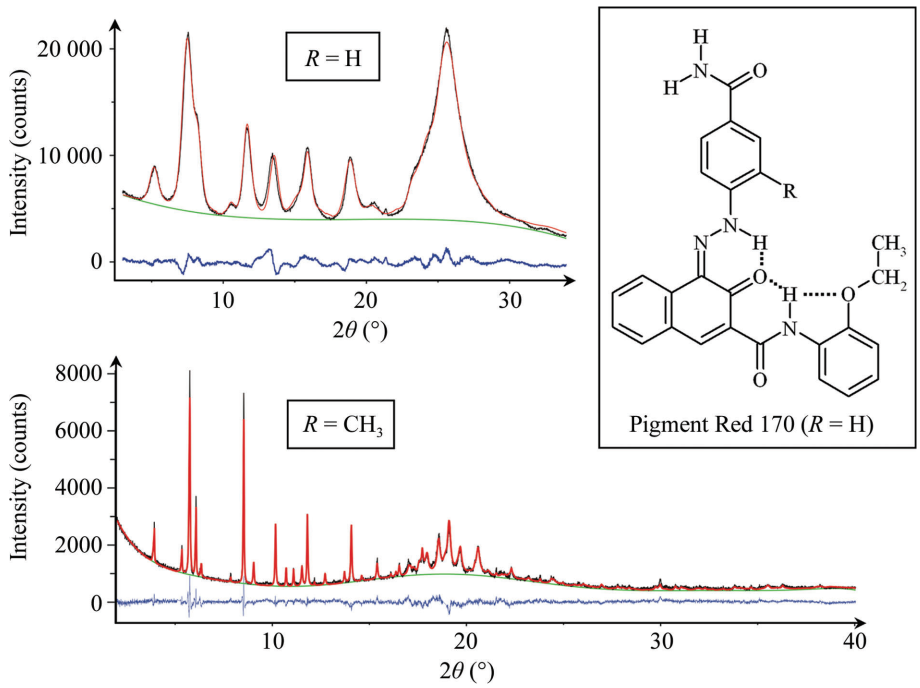

Figure 7.10.8

Structure determination of the nanocrystalline α-phase of Pigment Red 170 from powder data using an isostructural methyl derivative with improved crystallinity. Top, Rietveld plot of the α-phase of Pigment Red 170 (R = H); bottom, methyl derivative (R = CH_3). Experimental diffractograms are in black, the calculated diffractogram is in red, the background is in green and difference curves are in blue. Wavelengths were 1.5406 Å (Cu $K\alpha_1$) for Pigment Red 170 and 1.149914 Å (synchrotron radiation) for the methyl derivative. The space group is $P2_12_12_1$, with Z = 4, a = 23.960 (9), b = 23.234 (9), c = 3.887 (1) Å for Pigment Red 170 and a = 24.6208 (9), b = 22.8877 (9), c = 3.9388 (2) Å for the methyl derivative.

7.10.2.6. *Investigation of local structures of nanocrystalline and amorphous organic compounds using pair-distribution function analyses*

7.10.2.6.1. *General*

There is no sharp boundary between crystalline, nanocrystalline and amorphous states. In an amorphous sample the molecules can be ordered, despite the absence of Bragg reflections. For example, an organic compound with a domain size of 10 nm corresponding to about 5 × 5 × 5 unit cells with 500 molecules will not cause a single visible peak in the X-ray powder pattern; nevertheless, the molecules have a given conformation and form an ordered arrangement with a defined local structure.

Local structures in crystalline, nanocrystalline and amorphous organic compounds, including pharmaceuticals, agrochemicals, pigments and optoelectronic materials, can be investigated by pair-distribution function (PDF) analysis.

The pair-distribution function (also called the 'radial distribution function') represents the probability $G(r)$ of finding two atoms with an interatomic distance r. The PDF is weighted with the scattering power of the two atoms and is summed over all atom–atom pairs. The PDF contains intramolecular as well as intermolecular atom–atom distances. PDF curves are derived by Fourier transformations from carefully measured powder diffractograms. The method itself is explained in Chapter 5.7.

Applications to organic compounds include the following.

(i) The investigation of local structures and packing motifs in nanocrystalline and amorphous compounds.
(ii) The identification of polymorphic forms in nanocrystalline and amorphous compounds.
(iii) The investigation of the actual atomic and molecular arrangements in disordered structures.
(iv) To determine whether a powder is a co-crystal or a physical mixture of the individual compounds.
(v) The detection of crystal seeds in an amorphous powder. The commencement of crystallization is visible in the PDF at an earlier stage than in the powder diagram itself.

PDF analyses are widely used for inorganic compounds, for example glasses, liquids, amorphous or highly disordered materials, quasicrystals *etc.* (Neder & Proffen, 2009; Egami & Billinge, 2012). The application of PDF methods to organic compounds is at present (2018) in its infancy. The generation of a PDF curve from powder diffraction data is possible with programs such as *PDFgetX3* (Juhás *et al.*, 2013). The simulation of PDF curves from a structural model can be achieved, for example with *DISCUS* (Neder & Proffen, 2009), *RMCprofile* (Tucker *et al.*, 2007), *PDFgui* (Farrow *et al.*, 2007), *DiffPy-CMI* (Juhás *et al.*, 2015) or *TOPAS* (Coelho, 2018) (see Fig. 7.10.9). The full fitting of a structural model of an organic crystal structure to a PDF curve using restraints for bond lengths, bond angles and planar groups, such as in a Rietveld refinement, is nowadays becoming possible (Prill *et al.*, 2016).

7.10.2.6.2. *Example: nanocrystalline phase of Pigment Yellow 213*

Pigment Yellow 213 is an industrial hydrazone pigment used for automotive coatings. The compound exhibits two polymorphs (Fig. 7.10.10). The brown β-phase is obtained directly from the synthesis. Solvent treatment for 3 h at 423 K leads to the desired greenish-yellow α-phase. The crystal structure of the α-phase could be solved by a combination of X-ray powder diffraction, electron diffraction and lattice-energy minimizations (Schmidt, Brühne *et al.*, 2009). The molecules are almost planar and form a layer structure with an interlayer distance of 3.3 Å (Fig. 7.10.11).

The metastable β-phase is a nanocrystalline powder. The structures of both phases were investigated by PDF analyses. Powder patterns were carefully recorded with a short wavelength

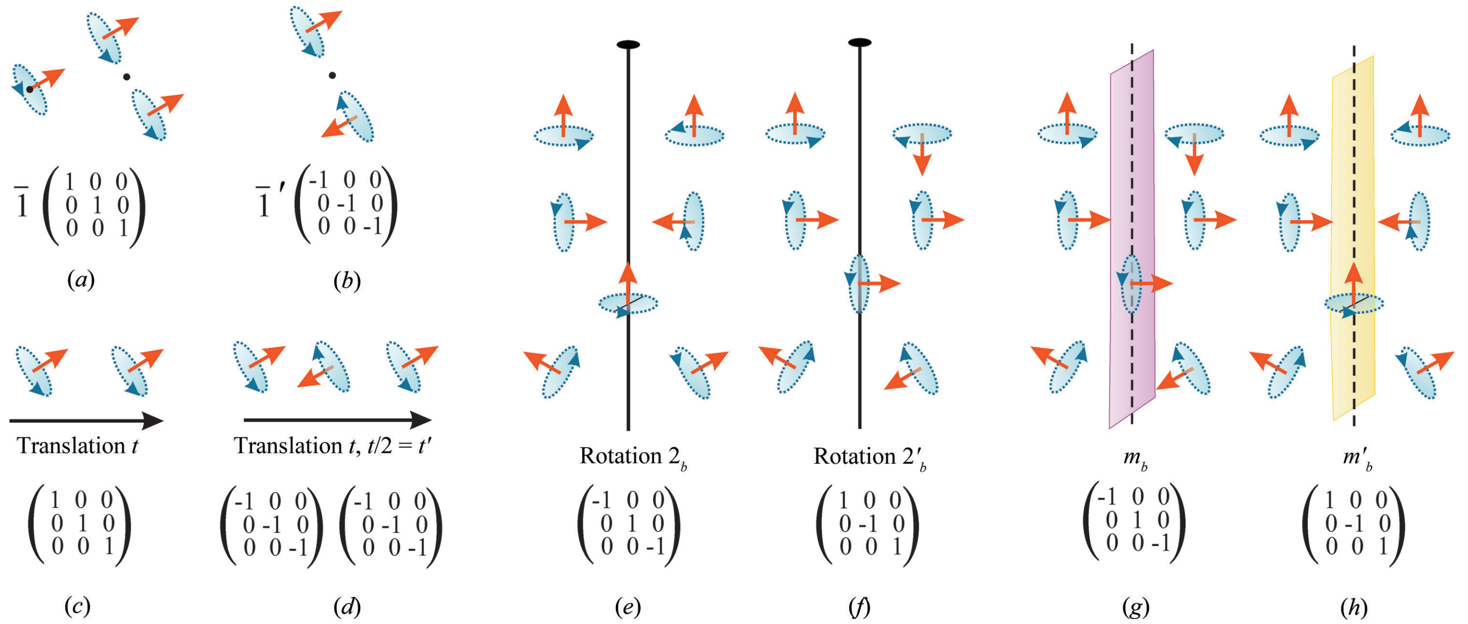

Figure 7.13.18

Selected magnetic symmetry and antisymmetry elements that Dannay *et al.* (1958) first applied to magnetic symmetry. (*a*) Inversion $\bar{1}$; (*b*) anti-inversion $\bar{1}'$; (*c*) translation *t*; (*d*) anti-translation *t*′; (*e*) rotation 2; (*f*) anti-rotation 2′; (*g*) reflection *m*; and (*h*) anti-reflection *m*′.

ferromagnetic moments have a ferromagnetic component and an antiferromagnetic component.

Collinear antiferromagnetic ordering. An example of collinear antiferromagnetic ordering is shown in Fig. 7.13.16(*d*). In this case there is only one type of ion (or atom), located in equivalent crystallographic positions and having equal moment amplitudes in an antiparallel orientation.

Canted antiferromagnetic ordering. Fig. 7.13.16(*e*) shows an example of a canted non-collinear antiferromagnetic order in which the moments tilt in such a way that both the $\mathbf{M}_x$ and $\mathbf{M}_y$ directions have antiparallel components. The magnetic unit cell has parameters that are double those of the nuclear unit cell.

A7.13.1.2. The 36 magnetic lattices and 1651 Shubnikov groups

The types of magnetic lattices are shown in Fig. 7.13.17. They are similar to the familiar crystal lattices in that they represent identical chemical entities, but the associated magnetic moments have the same amplitude and opposite orientation. The first row of the figure shows five types of white lattices: *P* (primitive), *C* (*C*-face centred), *A* (*A*-face centred), *F* (all-face centred) and *I* (body centred). All the white lattices represent ferromagnetic ordering of the moments. A white-and-black (W&B) lattice can be thought of as containing two lattices of the same type, one of which is termed 'white' and the other 'black'. The origin of the black lattice can be located at the centre of a face or at an edge, or at the body centre of the white lattice. For example, Fig. 7.13.17(*e*) indicates a white *I* lattice combined with a black *I* lattice with origin at *c*/2 of the white lattice, resulting in the W&B lattice I_c of Fig. 7.13.17(*c*). The W&B lattices are expressed by two-letter symbols in which the symbol (*P*, *C*, *A*, *I* or *F*) of the W lattice is followed by a subscript (*A*, *a*, *C*, *c*, *I* or *s*) which indicates the location of the origin of the black lattice. The capital subscript letters *A*, *C* and *I* indicate that the origin of the B lattice is at the *A*-face centre (0, *b*/2, *c*/2), *C*-face centre (*a*/2, *b*/2, 0) and at the body centre (*a*/2, *b*/2, *c*/2) of the white lattice, respectively. The lower-case subscript letters *a* and *c* indicate that the origin of the black lattice is at the centre of the *a* axis (*a*/2) and *c* axis (*c*/2) of the white lattice, respectively. For example, the lattice P_C is a combination of a *P* W lattice with a *P* B lattice with the origin at the *C*-face centre ($\frac{1}{2}$, $\frac{1}{2}$, 0) of the W lattice, while P_c indicates that the origin of the *P* B lattice is at *c*/2. These types of magnetic lattices, when applied to the seven crystal systems, give a total of 36 magnetic lattices, of which 14 are pure white and 22 are W&B lattices (see Table 7.13.3).

A7.13.1.3. Magnetic symmetry and antisymmetry operations

Magnetic symmetry elements include all the symmetry elements of the nuclear structure plus the corresponding anti-symmetry elements that are produced by adding the time (or current) reversal operation *R*. Selected typical elements of symmetry and antisymmetry and their symmetry-operation matrices are shown in Fig. 7.13.18. The operation of an element of antisymmetry can be performed as a normal symmetry operation followed by a reversal in direction.

A7.13.1.4. Magnetic reflection conditions for centred lattices

Table 7.13.4 lists the possible neutron magnetic reflection conditions related to the magnetic lattices illustrated in Fig. 7.13.17. The results are obtained by evaluating the neutron magnetic structure factor for F_{hkl} = 0 and are confirmed by computations using the program *GSAS* (Larson & Von Dreele, 2004). The conditions for systematic extinctions of magnetic reflections for glide planes and screw axes were reported by Ozerov (1967).

Effects of spin orientation in magnetic structures. Fig. 7.13.3 is a schematic view of the definition of the vectors relevant to the evaluation of the magnetic structure factor. In addition to the magnetic reflection conditions for centred lattices, glides and screws, systematic absences can also be observed when the condition $F_{hkl} = 0$ occurs because the magnetic spin $\mathbf{K}$ is parallel to the scattering vector $\boldsymbol{\varepsilon}$ for a class of reflections *hkl*. In this case, the angle α between the scattering and the magnetization vectors is zero and, consequently, $|q| = \sin\alpha = 0$.

Ambiguous spin orientation. Shirane (1959) showed that ambiguous spin structures can be deduced from NPD data, and concluded that: (i) no information can be obtained about the spin